1   **Midkine Attenuates Aβ Fibril Assembly and Amyloid Plaque Formation**

2

3   Masihuz Zaman[1,2#], Shu Yang[1,2,9#], Ya Huang[1,2#], Jay M. Yarbro[1,2], Yanhong Hao[1,2], Zhen Wang[1,2],

4   Danting Liu[1,2], Kiara E. Harper[1,2], Hadeer Soliman[1,2], Alex Hemphill[1,2], Sarah Harvey[1,2], Shondra

5   M. Pruett-Miller[3,4], Valerie Stewart[2], Ajay Singh Tanwar[1], Ravi Kalathur[1], Christy R. Grace[1], Martin

6   Turk[1], Sagar Chittori[1], Yun Jiao[1,2], Zhiping Wu[1,2], Anthony A. High[5], Xusheng Wang[5], Geidy E.

7   Serrano[6], Thomas G. Beach[6], Gang Yu[7], Yang Yang[8]*, Ping-Chung Chen[1,2]*, Junmin Peng[1,2]*

8

9   [1]Department of Structural Biology, St. Jude Children's Research Hospital, Memphis, TN 38105,

10   USA

11   [2]Department of Developmental Neurobiology, St. Jude Children's Research Hospital, Memphis,

12   TN 38105, USA

13   [3]Center for Advanced Genome Engineering, St. Jude Children's Research Hospital, Memphis,

14   TN 38105, USA

15   [4]Department of Cell and Molecular Biology, St. Jude Children's Research Hospital, Memphis,

16   TN 38105, USA

17   [5]Center for Proteomics and Metabolomics, St. Jude Children's Research Hospital, Memphis, TN

18   38105, USA

19   [6]Banner Sun Health Research Institute, Sun City, AZ 85351, USA

20   [7]Department of Neuroscience, Peter O'Donnell Jr. Brain Institute, University of Texas

21   Southwestern Medical Center, Dallas, TX 75390, USA

22   [8]Department of Structural Biology, Van Andel Institute, Grand Rapids, MI 49503, USA

23 [9]Present address: Department of Medical Research Center, State Key Laboratory of Complex

24 Severe and Rare Diseases, Peking Union Medical College Hospital, Chinese Academy of

25 Medical Sciences & Peking Union Medical College, Beijing 100730, P. R. China.

26

27 [#]Equal contribution

28

29 *Correspondence: yyang@mrc-lmb.cam.ac.uk; ping-chung.chen@stjude.org; or

30 junmin.peng@stjude.org

31
32

Abstract

Proteomic profiling of Alzheimer's disease (AD) brains has identified numerous understudied proteins, including midkine (MDK), that are highly upregulated and correlated with Aβ since the early disease stage, but their roles in disease progression are not fully understood. Here we present that MDK attenuates Aβ assembly and influences amyloid formation in the 5xFAD amyloidosis mouse model. MDK protein mitigates fibril formation of both Aβ40 and Aβ42 peptides in Thioflavin T fluorescence assay, circular dichroism, negative stain electron microscopy, and NMR analysis. Knockout of *Mdk* gene in 5xFAD increases amyloid formation and microglial activation. Further comprehensive mass spectrometry-based profiling of whole proteome and detergent-insoluble proteome in these mouse models indicates significant accumulation of Aβ and Aβ-correlated proteins, along with microglial components. Thus, our structural and mouse model studies reveal a protective role of MDK in counteracting amyloid pathology in Alzheimer's disease.

47   Alzheimer's disease (AD), an irreversible and progressive neurodegenerative disorder, is the

48   primary cause of dementia[1]. Genetic studies have revealed disease-specific genes (APP, PS1,

49   PS2), high-risk genes (APOE4, TREM2, UNC5C), and a large number of risk loci associated with

50   amyloid, tau, endocytosis, and immunity[2-4]. The dysregulation in the AD proteome within the brain

51   is characterized by the accumulation of Aβ amyloid plaques[5], tau neurofibrillary tangles[6], and

52   other aggregated proteins, including TDP-43[7,8] and U1 snRNP[9-13]. The recent FDA approval of

53   lecanemab and donanemab[14,15], both being amyloid-targeting antibodies, lend support to the

54   amyloid cascade hypothesis. However, the limited clinical benefits for AD patients suggest the

55   presence of alternative disease mechanisms and imply that intervention at a late disease stage

56   may be insufficient.

57   Complementary to the genetic search for AD disease genes, we and others have

58   performed large-scale proteomic profiling, uncovering consistent protein alterations in post-

59   mortem AD brains across multiple large cohorts[16-23]. This has highlighted the deregulation of

60   numerous molecular pathways and protein co-expression modules. Remarkably, a subgroup of

61   proteins is highly upregulated and show a strong correlation with Aβ levels since the early

62   prodromal stage throughout disease progression, including midkine (MDK), pleiotrophin (PTN),

63   netrin 1 (NTN1), netrin 3 (NTN3) and the HTRA1 serine protease[16,19]. Interestingly, these protein

64   changes occur independently of their mRNA transcript levels, indicating post-transcriptional

65   regulation[16,19], such as protein turnover [24,25]. Moreover, these Aβ-correlated proteins have been

66   found in the detergent-insoluble, aggregated proteome, and within amyloid plaques in AD brains,

67   as confirmed by mass spectrometry-based profiling and immunohistochemical analyses[13,26-29].

68   However, the direct involvement of these Aβ-correlated proteins in plaque formation and AD

69   pathogenesis remains to be elucidated.

70   The MDK/PTN family of cytokines, comprising only two members[30], are among the most

71   closely Aβ-correlated proteins identified in proteomic analyses[16,19]. They are multifunctional

72   heparin-binding factors that promote growth, survival, and migration of various cell types,

73   including neurons and immune cells[30]. In 1993, MDK was reported to localize within the amyloid

74   plaques associated with AD[31]. Preliminary studies suggest that MDK might directly interact with

75   Aβ, displaying high affinity and potentially mitigating Aβ's toxic effects[32], but the study had not

76   received attention in the AD research field. Recent proteomic findings support MDK as a top

77   candidate for modulating AD pathogenesis[16,19], raising interest in fully exploring the role of MDK

78   in AD pathogenesis.

79   In this study, we have thoroughly characterized the impact of MDK on Aβ assembly in

80   various assays including Thioflavin T, circular dichroism, negative stain electron microscopy (EM),

81   and NMR, demonstrating that MDK protein inhibits the formation of Aβ fibrils. Importantly, the *Mdk*

82   gene knockout (KO) in the background of 5xFAD mice leads to the amyloid increase and

83   microglial activation. Further proteomic profiling of these mouse models reveals the accumulated

84   Aβ and related proteins in the brain of the 5xFAD/KO mice, supporting MDK's protective role

85   against amyloid pathology in AD.

86

87   **Results**

88   **MDK, a top Aβ-correlated protein in human brain, attenuates Aβ fibril assembly**

89   Although MDK was identified within the senile plaques of AD patients by antibodies last century[31],

90   its role in AD has not been well investigated. Recent unbiased mass spectrometry (MS)-based

91   proteomic analyses have highlighted MDK as one of the top upregulated proteins highly correlated

92   with Aβ[16,19]. To verify these findings, we re-analyzed an AD proteomic dataset comprising 111

93   human cases[16], and performed Pearson correlation analyses of all identified proteins with Aβ and

94   tau levels (**Supplementary Data 1**). Strikingly, among more than 8,400 identified proteins, MDK

95   shows the best correlation with Aβ levels (R = 0.90) (**Fig. 1a**). In contrast, MDK displays a much

5

96 weaker correlation with tau (R = 0.29), consistent with the observation that the levels of Aβ and

97 tau do not strongly correlate in the human brain cases (R = 0.26). As a negative control, the

98 abundant housekeeping protein ubiquitin (Ub) exhibits essentially no correlation with Aβ levels (R

99 = 0.05). In the 5xFAD amyloidosis mouse model (referred to as FAD for simplicity), which

100 overexpresses mutant human *APP* and *PSEN1* genes[33], MDK accumulation was higher in FAD

101 mice than in wild type (WT), as determined by western blotting of cortical brain lysates (**Fig. 1b**).

102 Immunohistochemical (IHC) staining and immunofluorescent co-staining with Aβ confirmed the

103 presence of MDK in plaque regions of both human brains (frontal cortex, **Fig. 1c, d**) and the FAD

104 mice (cortex, **Fig. 1e, f**). These findings not only confirm the strong Aβ-MDK association in human

105 but also suggest the FAD mice as a valuable model for studying the role of MDK in AD

106 pathogenesis.

107 Given previous reports that MDK protein directly binds to Aβ peptides[16,32], we investigated its

108 impact on Aβ fibrillization using recombinant human MDK in multiple biophysical assays. We

109 purified and characterized MDK proteins expressed in mammalian 293 cells and *E. coli*. MDK is

110 a secretory protein with its mature form containing five disulfide bonds (S-S, **Extended Data Fig.**

111 **1a, b**). The stained SDS gel indicated near homogeneity of recombinant MDK from either source

112 after breaking S-S bonds (**Fig. 2a**). We then examined the formation of disulfide bonds in the

113 proteins by both top-down and bottom-up mass spectrometry. As expected, the 293-expressed

114 MDK proteins contain all five S-S bonds (**Fig. 2b, c**), whereas the bacteria-expressed version

115 contains a mixture of three proteoforms with 5, 4, and 3 S-S bonds, with the 5 S-S bond form

116 showing the highest abundance (**Fig. 2d**). The bottom-up analysis validated that all S-S bonds

117 were formed with the anticipated Cys pairs (**Extended Data Fig. 1b, c**). We then evaluated the

118 effect of recombinant MDK from both sources on the aggregation of synthetic Aβ40 and Aβ42

119 peptides. The fibrillization process was monitored by the fluorescence of thioflavin T (ThT), which

120 increases upon binding to amyloid fibrils[34]. Although *E. coli*-expressed MDK contains mixed

6

121   disulfide-bonded forms, it effectively inhibited Aβ fibrillization, similar to 293-expressed MDK,

122   albeit with slightly less efficiency (**Fig. 2e, f, Extended Data Fig. 1d, e**). Given its comparable

123   inhibitory effect, *E. coli*-expressed MDK was used for subsequent biophysical and structural

124   studies due to its higher yield.

125   We then fully characterized the aggregation propensity of Aβ peptides with recombinant MDK and

126   the negative control protein Ub using thioflavin T assay, circular dichroism (CD) analysis, electron

127   microscopy imaging, and Nuclear magnetic resonance (NMR) spectroscopy. When incubating

128   Aβ40 peptide (5 μM) alone or with titrated MDK at concentrations ranging from 1 μM to 10 μM

129   (**Fig. 3a**), Aβ40 displayed a time-dependent increase in fibrillization with a lag phase, growth

130   phase and a final plateau. However, the fibrillization process was retarded by MDK with increased

131   lag time and decreased ThT fluorescence intensity in a dose-dependent manner. We further used

132   the AmyloFit software[35] to determine the effects of MDK on microscopic steps during Aβ

133   aggregation. The best fit revealed that MDK negatively impacts Aβ40 secondary nucleation rate

134   constant (k_2) and elongation constant (k_+), as both $\log_2(k_2)$ and $\log_2(k_+)$ values showed a linear

135   decrease with increasing MDK concentrations (**Fig. 3b**, **Extended Data Fig. 2a, b**). At low MDK

136   concentrations (0.03 μM and 0.1 μM), ThT kinetics of Aβ40 remained largely unchanged, whereas

137   at higher concentrations (1 μM and 3 μM), we observed consistent inhibitory effect (**Extended**

138   **Data Fig. 2d**).

139   ThT fluorescence measurements are supported by far-UV CD spectroscopy, which detects the

140   characteristic β-sheet structure of amyloid fibrils formed by peptide self-assembly. Consistently,

141   CD analysis after 24 h incubation confirmed the inhibitory effect of MDK on fibrillization (**Fig. 3c**).

142   Aβ40 alone transitioned from an unstructured random coil (0 h) to a β-sheet structure with a

143   characteristic minimum around 218 nm (**Extended Data Fig. 2f**). In contrast, with the addition of

144   MDK, Aβ40 largely retained its unstructured conformation, showing a negative peak near 200 nm,

145   similar to Aβ40 monomers in a time course analysis (**Extended Data Fig. 2g**). We repeated all

7

146   ThT and CD analyses using Aβ42 peptide, yielding similar results (**Fig. 3d, e, f, Extended Data**

147   **Fig. 2c, e, h, i**). Electron microscopy imaging was used to detect the morphology of amyloid fibrils

148   in Aβ-MDK samples. Amyloid fibrils were observed as end-point aggregates in samples of

149   Aβ40/Aβ42 peptide (5 μM) alone (**Fig. 3g, h**). In contrast, fibril formation was abolished in the

150   presence of high concentrations of MDK (10 μM, 2:1 molar ratio).

151   In negative control experiments, we validated highly purified Ub by an SDS gel and MS analysis

152   (**Extended Data Fig. 3a, b, c, d**) and then performed ThT, CD and imaging experiments under

153   similar conditions. Unlike MDK, Ub did not exhibit a noticeable inhibitory effect on Aβ aggregation

154   (**Extended Data Fig. 3e, f, g, h, i, j**). Moreover, it is important to note that neither MDK nor Ub

155   alone fibrillated under the same conditions, as confirmed by ThT binding assay, far-UV CD, and

156   negative EM staining (**Extended Data Fig. 4a, b, c, d ,e, f**). Together, these results indicate that

157   midkine effectively inhibits the formation of amyloid fibrils *in vitro*.

158   In spite of the inhibitory effect of MDK on Aβ aggregation, we observed that Aβ could still

159   assemble as fibrils in the presence of lower MDK concentrations, such as a 1:1 molar ratio, and

160   subsequently examined the presence of Aβ42 fibrils under this condition using negative stain

161   (**Extended Data Fig. 5a**). As recombinant Aβ fibrils assemble differently from endogenous Aβ

162   filaments found in human brains[36-40], we further investigated the presence of MDK in Aβ fibrils

163   extracted from human AD brains. Immunogold negative stain EM with the MDK antibodies

164   revealed that MDK molecules were clustered around the Aβ fibrils (**Extended Data Fig. 5b**).

165   Moreover, we utilized the AlphaFold-multimer prediction tool[41] to hypothesize possible Aβ-MDK

166   interacting interfaces, suggesting that the N-terminus of Aβ (residues 1-12) might interact with the

167   C-terminus of MDK (residues 74-80 and 84-89) (**Extended Data Fig. 5c, d**).

168

169   To further confirm the effect of MDK on Aβ fibrillization, we acquired ^{1}H-^{15}N HSQC NMR spectra

170   of ^{15}N-labeled monomeric Aβ40 (10 μM) with MDK titration (0, 5, and 10 μM, **Fig. 4a**). Reference

171   spectra were acquired prior to incubation, with amide cross peaks assigned to specific residues[42].

172   After 48 h, a notable disappearance of cross peaks suggested Aβ40 peptide fibrillization.

173   Remarkably, with MDK co-incubation at varying concentrations, the cross peaks re-appeared

174   although at reduced intensities. As the HSQC cross peak intensities correlate with monomeric Aβ

175   concentration[43], we quantified the cross peak intensities for each residue (**Fig. 4b**), and calculated

176   the averaged percentage relative to the pre-incubation reference of Aβ40. The MDK addition (5

177   μM and 10 μM) rescued the cross-peak intensities from 0.9±0.2% to 38.3±1.1% and 38.1±0.9%,

178   respectively (**Fig. 4c**). We also observed a similar impact of MDK on Aβ42 fibrillization using a

179   protocol of 24 h incubation (**Fig. 4d**). However, the same concentrations of MDK were less

180   effective in recovering Aβ42 cross peaks compared to Aβ40 (**Fig. 4e, f**). For example, the MDK

181   addition (5 μM and 10 μM) retrieved the cross-peak intensities from 4.8±0.5% to 12.8±0.8% and

182   21.8±0.8%, respectively. This aligns with our ThT, CD and negative stain EM data, supporting the

183   notion that Aβ42 is more aggregation prone than Aβ40[39]. In contrast, ubiquitin (10 μM) used as a

184   control did not restore the Aβ40/42 signal under similar experimental conditions, supporting the

185   specificity of MDK's inhibitory effect (**Extended Data 6a, b, c, d**). In summary, our comprehensive

186   biophysical characterization strongly supports that MDK can modulate Aβ fibrillization *in vitro*.

187

188   **Genetic deletion of *Mdk* gene in FAD mice increases amyloid plaques and microglial**

189   **activation.**

190   To investigate the role of MDK in Aβ fibrillization *in vivo*, we generated a mouse model with an

191   *Mdk* gene knockout by CRISPR-mediated deletion of 23 base pairs in exon 3 of the mouse

192   genome (**Fig. 5a**). The deletion was confirmed through genome sequencing and PCR analysis

193   (**Fig. 5a**), with the absence of MDK protein verified by western blot analysis (**Fig. 5b**) and mass

194 spectrometry (**Extended Data Fig. 7a, b**). In WT mouse brain, *Mdk* gene is mainly expressed

195 from astrocytes and oligodendrocyte progenitor cells based on published single-cell RNA

196 sequencing analysis[44] (**Extended Data Fig. 7c**). We crossbred this knockout line with the FAD

197 mice to produce offspring that were FAD mice with or without the *Mdk* knockout. The *Mdk*

198 knockout resulted in a marked increase in Aβ levels in the cortices of 12-month-old mice brains,

199 as shown by western blot analysis (**Fig. 5b**). ELISA analysis also indicated elevated accumulation

200 of Aβ40 and Aβ42 in both Sarkosyl-soluble and -insoluble fractions of mouse cortices in the

201 FAD/KO mice (**Fig. 5c, d**), whereas the ratio of Aβ40/Aβ42 was not significant changed

202 (**Extended Data Fig. 7d**). These biochemical findings indicate that *Mdk* gene knockout

203 contributes to the increased accumulation of two major Aβ species in the FAD genetic

204 background.

205 Next, we characterized the FAD/KO mice through immunostaining to evaluate the effects of *Mdk*

206 deletion on plaque formation and microglial activation in the brain. *Mdk* knockout led to increased

207 plaque density and area, as detected by X34 staining, a fluorescent dye that binds to β-sheet

208 structures in amyloid plaques[45], in the cortices of 12-month-old mouse brains of both male and

209 female mice (**Fig. 5e, Extended Data Fig. 7e, f, g**). This was accompanied by heightened

210 microglial activation, evidenced by increased microglial density and area (**Fig. 5f**). In subsequent

211 immunofluorescence staining studies, amyloid plaques detected by the Aβ antibody were found

212 to highly colocalize with MDK protein in FAD mice, and the MDK staining was absent in the

213 knockout mice (**Fig. 5g**). Additional co-staining with IBA1, a protein marker for microglia[46,47] ,

214 revealed a significant accumulation of microglia around the plaque areas (**Fig. 5g**), in agreement

215 with the observed increase in microglial density and area in the FAD/KO mice. These results

216 indicate that *Mdk* gene knockout leads to enhanced plaque formation and microglial activation in

217 the FAD mouse model.

218

219   To understand the impact of *Mdk* knockout in the FAD mice at the molecular level, we analyzed

220   the cortical brain proteome across four genotypes: WT (n = 8), KO (n = 8), FAD (n = 15), and

221   FAD/KO (n = 17) as shown in **Fig. 6a,** Employing a refined tandem-mass-tag coupled with two-

222   dimensional liquid chromatography and tandem mass spectrometry (TMT-LC/LC-MS/MS)

223   platform[13,48-50], we identified 154,013 peptides, corresponding to 9,441 protein groups (9441

224   genes) across all these samples with protein false discovery rate (FDR) below 0.01

225   (**Supplementary Data 2-3**). After loading bias correction (**Extended Data Fig. 8a**), principal

226   component analysis (PCA) and clustering analysis clearly separate distinct mouse groups,

227   indicating the high quality of the proteomic data (**Fig. 6b, Extended Data Fig. 8b**). As a positive

228   control, MDK protein levels were elevated in FAD mice compared to WT and reduced to noise

229   levels in knockout mice (**Fig. 6c**). In FAD mice, *Mdk* deletion led to a significant increase of Aβ

230   peptide levels (**Fig. 6c**), but did not affect the expression level of the full-length APP protein

231   (**Extended Data Fig. 8i, j**).

232   To identify the differentially expressed proteins (DEPs) among the four genotypes, we performed

233   an ANOVA analysis using a previously reported method[16] with two criteria: (i) an FDR value of

234   less than 5%, and (ii) a log2 fold change (FC) greater than twice the standard deviation (2 SD) in

235   any of the three pairwise comparisons: WT vs KO, FAD vs WT, or FAD/KO vs FAD (**Extended**

236   **Data Fig. 8c**). Following this analysis, a total of 818 DEPs were accepted (**Supplementary Data**

237   **4**). We then classified these DEPs into four whole proteome clusters (WPCs) using the weighted

238   gene co-expression network analysis (WGCNA)[51], followed by pathway enrichment analysis (**Fig.**

239   **6d, Supplementary Data 4-5**). The WGCNA program identified clusters of highly correlated

240   proteins based on the DEP data by calculating pairwise correlations to construct a network, and

241   applying a thresholding approach to emphasize strong correlation patterns. In detail, WPC1 (n =

242   493) exhibits a gradual increasing trend across the four genotypes from WT, KO, FAD to FAD/KO.

243   This cluster includes Aβ and Aβ-correlated proteins[16], such as Ntn1, Ptn, and Clu, as well as some

244   marker proteins for microglia and astrocytes: Trem2, Ctss, Olfml3, Csf1r, Gfap, Aqp4, Pla2g7,

245   and Gja1[52,53] (**Extended Data Fig. 8d**), and it is enriched in four representative pathways: APP

246   metabolic process, microglia activation, astrocyte activation, heparin binding and lipid catabolic

247   process (**Fig. 6e, Supplementary Data 6**). In contrast, WPC2 (*n* = 181) shows notable decrease

248   along the four genotypes, related to the pathways of calcium ion transmembrane transport,

249   vesicle-mediated transport in synapse, neurotransmitter secretion, cognition, and G protein-

250   coupled glutamate receptor signaling. Interestingly, this cluster includes the AD risk gene/protein

251   Bin1 that regulates calcium homeostasis and neuronal excitability[54,55].

252   In addition, both WPC3 (*n* = 72) and WPC4 (*n* = 72) display effects of *Mdk* knockout that are

253   independent of the FAD genetic background. Proteins in WPC3 increase in *Mdk* KO mice and are

254   enriched in six major pathways: small molecule catabolic process, lactone metabolic process,

255   GTPase regulator activity, SCF ubiquitin ligase complex, retrograde axonal transport and

256   regulation of Notch signaling pathway (**Fig. 6e, Supplementary Data 6**). For instance, Slc18a3

257   (the vesicular acetylcholine transporter) functions to transport acetylcholine into synaptic vesicles

258   during cholinergic neurotransmission, regulating cognitive functions such as learning and

259   memory, motor coordination, and synaptic plasticity[56]. WPC4 primarily consists of proteins that

260   are significantly downregulated due to *Mdk* knockout, enriched in the pathways of tetrapyrrole

261   metabolic process, ribosome disassembly, neurotrophin binding, adherens junction, myeloid cell

262   development and MLL1 complex. For example, Nbr1 is a selective autophagy receptor that

263   recognizes ubiquitinated proteins and damaged organelles, promoting their degradation through

264   the autophagy-lysosome pathway[57]. Overall, the protein alterations found in WPC3 and WPC4

265   likely reflect the developmental function of midkine, implicating a pleiotropic impact of *Mdk*

266   knockout. Nevertheless, within WPC1, we observed a distinct increase in Aβ and Aβ-correlated

267   proteins, along with the activation of microglia and astrocytes, supporting that *Mdk* knockout

268   exacerbates pathological severity.

269   Furthermore, we validated the enhanced pathology in FAD/KO mice by profiling the detergent-

270   insoluble proteome, which is enriched in aggregated proteins, across the four mouse genotypes.

271   A total of 169,864 peptides from 8,728 unique protein groups (8,728 genes, **Fig. 6f,**

272   **Supplementary Data 7**) were identified. After performing quality control analyses, such as

273   loading bias normalization and PCA (**Extended Data Fig. 8e, f**), we found that 314 DEPs were

274   elevated in the insoluble proteome of FAD/KO mice compared to FAD mice (**Extended Data Fig.**

275   **8g, Supplementary Data 7**). Remarkably, the FAD/KO mice showed an accumulation of Aβ and

276   other plaque-associated proteins in the insoluble proteome relative to FAD mice. A heatmap

277   highlights some of these proteins, consistently detected in both the whole and insoluble

278   proteomes, including Ntn1, Apoe, Ptn, Clu, Smoc1, Sfrp1, Sulf2, C4b and Scube1 (**Fig. 6g, h,**

279   **Extended Data Fig. 8h**). It should be noted that the expression of full-length APP in these mouse

280   lines was not affected by *Mdk* gene knockout in the whole proteome analysis (**Extended Data**

281   **Fig. 8i, j**).

282   In summary, the knockout of *Mdk* gene within the FAD mice resulted in an increase in Aβ and Aβ-

283   associated proteins, amyloid plaque formation, and microglial activation. This was substantiated

284   through experiments of western blotting, ELISA, immunostaining of brain tissues, and extensive

285   proteomic profiling of both the whole and detergent-insoluble proteomes in the brain.

286   **Discussion**

287   Midkine is one of the most correlated proteins with Aβ peptides in the proteomic analysis of post-

288   mortem human brain tissues of Alzheimer's disease. Our biophysical and NMR studies show that

289   MDK inhibits Aβ assembly and fibril formation *in vitro*. Consistently, functional *in vivo* analysis in

290   the FAD mouse model shows that CRISPR-mediated *Mdk* knockout leads to increased amyloid

291   deposition and concurrent microglial activation, which is further supported by deep profiling of

292   whole proteome and detergent-insoluble proteome in the brain.

13

293   MDK is a heparin-binding growth factor of ~15 kDa, conserved between mouse and human, with

294   87% protein sequence identity[30]. MDK consists of a signal peptide, an N-terminal domain involved

295   in receptor binding, and a C-terminal domain containing the heparin-binding site. Its structure is

296   stabilized by five intra-domain disulfide bonds, three in the N-terminal domain and two in the C-

297   terminal domain. We expressed recombinant His-tagged MDK proteins in mammalian 293 cells

298   and *E. coli*, and removed the tag by proteases after purification to avoid functional interference

299   (**Extended Data Fig. 1a**). Our top-down and bottom-up MS analysis confirmed the protein

300   sequences and revealed that the MDK expressed in mammalian 293 cells contained all five

301   expected disulfide bonds, while the *E. coli*-expressed version existed as a mixture of three forms,

302   with the five-disulfide form being the most prevalent. The *E. coli*-expressed version showed

303   slightly lower activity in the ThT assay, potentially due to reduced stability in the other two forms

304   lacking one or two disulfide bonds. However, its overall activity remained comparable to that of

305   the 293-expressed MDK. CD and NMR analyses further confirm the inhibitory effect of *E. coli*-

306   expressed MDK on Aβ assembly.

307   Our results suggest that MDK targets the processes of elongation and secondary nucleation,

308   which are specific pathways during Aβ aggregation. The Aβ aggregation kinetics starting from

309   monomers is inherently complex, including a lag phase, during which a small but critical

310   concentration of amyloid oligomers accumulates, followed by an elongation phase, leading to fibril

311   formation. Additionally, a secondary nucleation pathway occurs on the surface of existing fibrils,

312   promoting further fibril formation[58,59]. Using the AmyloFit interface[35], we globally fitted our kinetic

313   data to different models (primary nucleation, secondary nucleation, and fragmentation), with

314   secondary nucleation providing the best results. MDK may inhibit Aβ fibrillation similar to sTREM2,

315   which selectively binds to Aβ and primarily suppresses secondary nucleation, with minimal impact

316   on primary nucleation[60]. sTREM2 interacts with Aβ fibrils via two distinct structural surfaces to

317   inhibit secondary nucleation, and similarly, MDK may recognize Aβ through specific interaction

14

318   sites, potentially modulating fibril formation via comparable mechanisms. Although the exact Aβ-

319   MDK binding interface remains unknown, *in-silico* modeling by AF2 multimer predicts that MDK

320   interacts with Aβ via its C-terminal heparin-binding domain.

321   Targeting Aβ aggregation is a key therapeutic strategy to slow disease progression. The success

322   of Aβ antibody therapy[14,15] underscores the importance of Aβ assembly, particularly protofibrils,

323   in AD pathogenesis and highlights the need for precise Aβ conformation targeting to improve

324   therapeutic outcomes[61]. Further research is needed to examine the Aβ-MDK interaction at an

325   atomic level, which could provide critical mechanistic insights for the rational design of effective

326   therapeutic strategies.

327   In addition to its role in inhibiting Aβ assembly, MDK functions as a growth factor that promote

328   neurite outgrowth and cell survival[30]. It has been shown to interact with several membrane

329   receptors, including PTPζ[62], LRP-1[63], integrins (α6β1 and α4β1)[64], Neuroglycan C[65], ALK[66], and

330   Notch-2[67], regulating development, cell migration and inflammation during brain injury[30]. Although

331   most of these MDK receptors are underexplored in AD, LRP-1 is a receptor for the risk factor

332   *APOE* in AD development[68]. In our proteome analysis of *Mdk* KO mice, we did not observe

333   significant changes in the protein levels of these known MDK receptors. However, we identified

334   alterations in a subset of proteins (WPC3 and WPC4) resulting from the knockout of the *Mdk*

335   gene, independent of the FAD genetic background. These perturbed proteins may also influence

336   AD-related pathology in the knockout mice.

337   When knocking out the *Mdk* gene in FAD mice, we found a noticeable increase in its paralog

338   protein Ptn in the mouse brain. This upregulation may be driven by at least two possible

339   mechanisms: (i) *Mdk* knockout induces Ptn upregulation at the transcriptional level, (ii) *Mdk*

340   knockout leads to Aβ accumulation, which in turn slows the turnover of Aβ-associated proteins,

341   including Ptn. The first mechanism may not apply to *Mdk* knockout mice without amyloid

342   pathology, as the Ptn protein level remains unchanged under these conditions (**Fig. 6h**).

343   Interestingly, the second mechanism was recently suggested in a proteome turnover study, which

344   explained some RNA-protein inconsistencies in FAD mice[24], highlighting delayed protein turnover

345   within the amyloid microenvironment. To fully elucidate the relationship between Mdk and Ptn and

346   their contribution to AD pathology, we plan to further investigate these mechanisms using double-

347   knockout mouse models.

348   During the revision of this manuscript, Levites et al. published a proteomics study on human AD

349   cases, complemented by systematic IHC validations and some functional studies[69]. Their study

350   focused on a conserved network termed the "Aβ amyloid responsome," which includes MDK and

351   its paralog PTN. They reported that commercially available MDK and PTN proteins promoted

352   fibrillation in a ThT assay, and virus-mediated overexpression of MDK and PTN enhanced

353   parenchymal Aβ amyloid deposition and CAA in CRND8 mice, a transgenic model overexpressing

354   mutant human APP[70]. In contrast, using fully characterized MDK protein from multiple sources,

355   we clearly demonstrate its negative impact on Aβ assembly through an array of detailed

356   biophysical, EM imaging, and NMR studies. The discrepancy in mouse studies may result from

357   differences in models, perturbations, and other experimental variables. Despite these differences,

358   both studies suggest that MDK modulates amyloid accumulation, underscoring the need for

359   further research to reconcile these findings.

360   Taken together, our findings demonstrate that MDK disrupts Aβ fibril assembly, and its genetic

361   deletion exacerbates plaque accumulation in the FAD mouse model. Given the extended

362   prodromal period before clinical AD onset, early Aβ accumulation may activate compensatory

363   mechanisms to mitigate Aβ toxicity. Our research suggests that MDK may serve as one such

364   factor, providing protective effects against Aβ-induced toxicity and contributing to resistance

365   against amyloid pathology. Further exploration of the MDK pathway could offer new insights into

366   modulating AD disease progression.

367

16

Acknowledgments

Contributions

J.P., P.-C.C., G.Y. M.Z. conceived this project. M.Z., Y.Y, J.M.Y., Y.H., A.S.T., R.K., C.R.G., M.T., and S.C. engaged in biophysical experiments. S.Y., Z.Wang, K.E.H., H.S., A.H., S.H., Y.J., and P.-C.C. performed biological experiments. P.-C.C., S.Y., Y.J., S.M.P.-M., and V.S. generated and bred the mouse models. S.Y., Z.Wang, D.L., Y, H., Z.Wu, A.A.H., X.W. contributed to the mass spectrometry-based proteomics analysis. G.E.S. and T.G.B. characterized and provided human brain samples. M.Z., Y.H., P.-C.C. and J.P. wrote the manuscript.

Competing interests

The authors declare no competing interests.

Methods

All experiments performed in this study comply with all relevant ethical regulations. All animal experiments were approved by the Institutional Animal Care and Use Committee (IACUC) at St Jude Children's Research Hospital.

Statistics and reproducibility. Sample sizes were not predetermined using statistical methods; however, they closely resembled those reported in previous publications [68-70]. While the assumption of normal data distribution was made, formal testing for normality was not analyzed. Variances were assessed using the F-test. An unpaired Student's *t*-test was used for comparisons between two groups with equal variance, while an unpaired Welch's *t*-test was used for groups with unequal variance. For proteomics data, *p*-values were calculated by moderated *t*-test in the limma package, followed by false discovery rate analysis by the Benjamini-Hochberg procedure. Animals were utilized whenever available without randomization. Outliers were removed using the Dixon's Q-test. The investigators were blinded to genotype information during the quantitation of immunostaining for plaque and microglia.

Human brain samples. Human postmortem brain tissue samples (frontal gyrus) for Western blot analysis were provided by the Brain and Body Donation Program at Banner Sun Health Research Institute. Clinical and pathological diagnoses were based on the established criteria[71].

Mouse model. All mice (C57BL/6J) were housed under a 12-h light: 12-h dark cycle at 22-25 °C and 40%-60% humidity. *Mdk* knockout mice were generated using CRISPR-Cas9 technology to partially delete coding region in the genome to cause frame shift mutation. Briefly, dual gRNAs were designed with *in silico* off-target analysis to determine highly unique spacer sequence with at least 3 bp of mismatch to any other site in the mouse genome. In addition, we also consider the targeted region covered among all isoforms, and select CAGE257.MDK.g2 (5'-

416 UGCGGCAUGGGCUUCCGCGA- 3') and g14 (5'-GCACCUUGCAAUGGACGCGC-3').

417 Precomplexed ribonucleic proteins (RNPs) consisting of 25 ng/μl of each sgRNA (Synthego) and

418 50 ng/ μl SpCas9 mRNA (Trilink) were injected into the cytoplasm of C57BL/6J fertilized zygotes

419 and transferred to CD-1 pseudo-pregnant fosters. Resulting animals were genotyped by targeted

420 next generation sequencing using primers CAGE257.F: 5'-

421 GTGAGGCAGGCCGTGTGACCAAGTG-3' and CAGE257.R:5'-

422 TGCAGTCGGCTGATGGGAGAGTGGC-3' and analyzed using CRIS.py[72,73]. Founder animals

423 with out-of-frame mutations were backcrossed to C57BL/6J mice for two generations. A founder

424 carrying a 23 bp deletion in exon 3 was selected for the study. Genotyping of the knockout mice

425 was carried out by PCR with primers specific for WT (F: 5'-CTTCCGCGAGGGTACCTG-3', R:

426 5'-TATTCGCTGACCTTTGGTCTT -3') and the *Mdk* knockout (F: 5'-

427 GCACGCCATGTCCTTAACTTT-3', R: 5'-TGGGTCTGGGCCCATG-3'). FAD mice (B6.Cg-

428 Tg(APPSwFlLon,PSEN1*M146L*L286V)6799Vas/Mmjax) were obtained from Jackson

429 Laboratory (MMRRC_034848-JAX) and underwent backcrossing with C57BL/6J for at least 10

430 generations. *FAD/Mdk^{-/-}* (FAD/KO) mice were generated by crossing with *FAD/Mdk^{+/-}* with *Mdk^{+/-}*

431 mice. In mouse experiments, similar numbers of male and female animals were utilized.

432

433 **Western blotting.** Protein lysates underwent separation via 4-20% Tris-Glycine gel and transfer

434 to 0.22 μm nitrocellulose membranes. Blots underwent a 1 h blocking with 3% BSA for MDK or

435 5% skim milk for other targets. The following primary antibodies were incubated overnight at 4°C:

436 anti-mouse MDK (1:1000, sheep polyclonal, R&D, AF-7769), anti-Aβ (1:1000, mouse monoclonal,

437 clone 82E1, IBL, 10323), and anti-β-tubulin (1:5000, rat monoclonal, clone YOL1/34, abcam,

438 ab6161). After three 5-min washes, blots were exposed to secondary antibodies conjugated with

439 HRP (1:40,000, Jackson ImmunoResearch) for 1 h at 21 °C, followed by another three 5-min

440 washes. Chemiluminescence was developed by using either the SuperSignal West Pico PLUS or

441 Femto substrate (Thermo Fisher Scientific) and detected by ChemiDoc system (Bio-Rad).

442

443   **Recombinant MDK expression and purification from *E. coli*.** The MDK construct (22-143 aa)

444   was overexpressed in BL21 (DE3) Rosetta 2 cells. A single colony was used to cultivate a starter

445   culture overnight. Subsequently, 10 ml of the starter culture was used to inoculate 1 L of 2XYT

446   medium containing 50 µg/ml kanamycin and 35 µg/ml chloramphenicol. The inoculation took

447   place at 37°C with agitation at 220 rpm until the cell density reached an OD_{600} of approximately

448   0.8.Protein overexpression was induced by adding 0.5 mM isopropyl β-D-thiogalactopyranoside

449   (IPTG), and the culture was further incubated at 18°C for 16 h. Cells were harvested by

450   centrifugation at 5000 rpm for 15 min at 4°C, and the cell pellet was frozen at -80°C until use. The

451   pellet was resuspended in lysis buffer (20 mM HEPES, pH 7.4, 500 mM NaCl, 5% glycerol)

452   supplemented with an EDTA-free complete protease inhibitor cocktail tablet (Roche).

453   Cell disruption was performed using a cell disruptor (Constant Systems Ltd.) at 20.0 kPSI

454   pressure in two rounds of lysis. The resulting lysate was cleared by centrifugation at 20,000 rpm

455   for 30 min at 4°C and subsequently applied to a gravity column following a 30-min incubation with

456   pre-equilibrated Ni-NTA resin at 4°C. The column was washed with 10 column volumes (CV) of

457   wash buffer A (20 mM HEPES, pH 7.4, 500 mM NaCl, 12.5 mM imidazole, and 5% glycerol),

458   followed by 10 CV of wash buffer B (20 mM HEPES, pH 7.4, 500 mM NaCl, 50 mM imidazole,

459   and 5% glycerol). The protein was eluted with buffer containing 20 mM HEPES, pH 7.4, 500 mM

460   NaCl, 250 mM imidazole, and 5% glycerol.

461   Eluted fractions were analyzed by SDS-PAGE using a 4–20% gel. Subsequently, the elution

462   fractions were combined, and the His-tag was cleaved from the protein using tobacco etch virus

463   (TEV) protease overnight at 4°C. The cleaved protein was further purified by size-exclusion

464   chromatography using a Superdex 75 16/600 column (Cytiva) equilibrated with 50 mM Tris-HCl,

465   pH 7.5, 500 mM NaCl, and 5% glycerol. Finally, the protein fractions were pooled, concentrated

466   to the desired concentration, flash-frozen in liquid nitrogen, and stored at -80°C for subsequent

467   experiments.

20

468

469 **Recombinant MDK expression and purification from mammalian 293 cells.** The MDK gene

470 with an Igκ secretion signal and followed by a His tag, was cloned into the pcDNA 3.4 vector.

471 Recombinant protein was expressed in Expi293F cells (Thermo Fisher Scientific, A14527)

472 through transient transfection using the ExpiFectamine™ 293 Transfection Kit. For the

473 transfection, Expi293F cells at a density of 3×10^6 cells/ml were treated with 1 mg of DNA plasmid

474 per liter of cells. The transfected cells were incubated at 37°C in an orbital shaker set to 140 rpm

475 with 5% CO_2 for ~24 h. Then the cells were centrifuged at 1000 x g for 15 mins, and the

476 supernatant was collected. This supernatant was applied to pre-equilibrated Ni-NTA resin

477 (Qiagen) and incubated for 1 h at 4°C. The incubated resin was then collected by centrifugation

478 at 1500 rpm for 10 mins at 4°C and washed with 10 column volumes (CV) of wash buffer A (20

479 mM HEPES, pH 7.4, 500 mM NaCl, 12.5 mM imidazole, and 5% glycerol), followed by 10 CV of

480 wash buffer B (20 mM HEPES, pH 7.4, 500 mM NaCl, 50 mM imidazole, and 5% glycerol). The

481 protein was eluted using a solution of 20 mM HEPES, pH 7.4, 500 mM NaCl, 250 mM imidazole,

482 and 5% glycerol. The eluted fractions were analyzed by loading onto a 4-20% SDS-PAGE gel.

483 The MDK-containing fractions were pooled, and the His tag was cleaved from the protein

484 overnight at 4°C using tobacco etch virus (TEV) protease. The cleaved protein was then further

485 purified by size exclusion chromatography utilizing a Superdex 75 10/300 Increase column

486 (Cytiva), which was pre-equilibrated with 20 mM sodium phosphate, pH 7.2, 500 mM NaCl, and

487 5% glycerol. Finally, the protein fractions collected from the column were pooled, concentrated,

488 flash-frozen in liquid nitrogen, and stored at -80°C for subsequent experiments.

489

490 **MS analysis of recombinant MDK and Ub proteins.** Purified MDK (350 µg/mL, 50 mM Tris-

491 HCl, pH 8.0) was alkylated with 2 mM iodoacetamide for 1 h at RT in the dark to block any potential

492 free thiols. The proteins were then desalted using C18 StageTips (Thermo Scientific) and dried

493 before being re-dissolved in 5% FA for LC-MS analysis. Ubiquitin was prepared in 5% FA directly.

21

494   LC-MS acquisition was performed using an Ultimate 3000 RSLCnano System coupled to an Q

495   Exactive HF Orbitrap MS (Thermo Fisher Scientific). Samples were separated on a C18 column

496   (75 µm x 20 cm) packed with 1.9 µm C18 resin (Dr. Maisch GmbH). Mobile phase A consisted of

497   0.2% formic acid, 5% DMSO; Mobile phase B consisted of solvent A plus 65% ACN. The gradient

498   program varied from 20 to 30 min for different proteins. MS data were acquired with a full MS

499   scan with m/z range of 410-1200 or 410-2000 for different proteins, all at R = 240000 (m/z = 200).

500   The resulting raw data were deconvoluted using the Thermo BioPharma Finder Software to obtain

501   the isotopic mass of the intact protein.

502   For bottom-up analysis, the same samples were alkylated with 2 mM iodoacetamide for 1 h at RT

503   in dark. Subsequently, the proteins were digested in two rounds with trypsin at an enzyme-to-

504   protein ratio of 1:10 (w/w) at 21 °C for at least 8 h. The resulting peptides were desalted using

505   C18 Stage Tips (Thermo Fisher Scientific). LC-MS/MS acquisition was performed using an

506   Ultimate 3000 RSLCnano System coupled to a Q Exactive HF Orbitrap MS (Thermo Fisher

507   Scientific). Samples were redissolved in 5% FA and loaded onto a C18 column (75 µm x 20 cm)

508   packed with 1.9 µm C18 resin (Dr. Maisch GmbH). Mobile phase A consisted of 0.2% formic acid

509   and 5% DMSO, while mobile phase B consisted of solvent A plus 65% ACN. LC separation was

510   performed with a 5-50% buffer B gradient in 25 min. MS analysis was operated in data-dependent

511   acquisition mode with a full MS scan between m/z 410-1200 at R = 60000 (m/z = 200), followed

512   by 10 MS/MS scans at R = 60000 (m/z = 200) with an isolation width of 1.0 m/z. The AGC target

513   for MS and MS/MS scan were set to 3×10^6 and 1×10^6, respectively, with maximum injection

514   time of 50 ms and 110 ms. The precursors with charge states of 2 to 7 were selected for HCD

515   fragmentation with normalized collision energy set to 30%. Dynamic exclusion was set to 10 sec.

516   All samples were analyzed in technical triplicates.

517   For the identification of disulfide bonds, the raw data were analyzed using pLink 2.0 software

518   (version 2.3.11)[74] with the following parameters: Cross-linker, SS; Database, FASTA file

519   constructed based on the MDK sequence; Precursor tolerance, 10 ppm; Fragment tolerance, 10

520   ppm; Number of missed cleavages, 0; Peptide mass, [200, 6000]; Peptide length, [2, 60]; Fixed

521   modification, carbamidomethylation for cysteines; Filter tolerance, ± 10 ppm; FDR, 1% at PSM

522   level. Specifically, the identification of Cys17 and Cys25 containing cross-linked peptides were

523   manually checked, as peptide sequence between Cys17 and Cys25 cannot be cleaved by trypsin.

524   This may allow for the formation of two disulfide bonds among 3 peptides, such as the

525   EGTC$_{41}$GAQTQR–GGPGSEC$_{17}$AEWAWGPC$_{25}$TPSSK–C$_{50}$R, which could not be identified by

526   pLink2. Peptide quantification was performed using the peak area of precursors with the highest

527   intensity. Data were further normalized using the intensity of one trypsin peptide "VATVSLPR".

528   The top-five most abundant disulfide bonds were shown in figures.

529

530   **ThT fluorescence assay.** Aβ40 and Aβ42 (rPeptide, #A-1153-1, and #A-1163-2) with a purity of

531   > 97%. Each peptide vial was suspended in 1,1,1,3,3,3-hexafluoro-2-propanol (HFIP), incubated

532   for an h to disperse any preexisting aggregates. Further, these samples were aliquoted and

533   carefully dried in a nitrogen stream and stored in -80°C. Aliquots of purified Aβ species were

534   dissolved in 10 mM NaOH to a concentration of 2 mg/ml followed by 10 min cooling and sonication

535   in an ice water bath for 1 min. The concentration of the final monomeric sample was quantified

536   by nanodrop at 280 nm. MDK protein purified from *E. coli* and 293 cells was dialyzed overnight in

537   50 mM Tris-HCl buffer, pH 7.5 and final concentration was determined by absorbance

538   measurements at 280 nm. Further, the freshly dissolved Aβ peptides were diluted to 5 µM in

539   absence and presence of different concentrations of purified MDK containing 50 mM Tris-HCl, pH

540   7.5 buffer containing 20 µM Thioflavin. 100 µl of solution was added into 96-well half area, solid

541   bottom, clear, sterile, microtiter plates and sealed with sealing tape to prevent evaporation. All

542   kinetic experiments were performed at 37°C under quotient conditions at every 5 min in a

543   Clariostar plate reader (BMG Labtech) using an excitation and emission wavelengths of 440 and

544   480 nm respectively. All these assays were performed in three replicates. The Aβ peptides were

545   diluted to 5 µM at a final concentration in absence and presence of human Ub protein (5 and 10

546 µM, Bio-Techne R & D systems, U-100H-10M) to monitor aggregation kinetics as described

547 above. Aggregation kinetics of MDK and Ub at different concentrations in the same buffer (50 mM

548 Tris-HCl) with fixed ThT concentrations (20 µM) were also recorded.

549

550 **Circular dichroism spectroscopy.** All CD spectra were recorded on a JASCO-1500

551 Spectrophotometer at a wavelength of 195 - 250 nm with a step size of 0.1 nm, 1 nm bandwidth,

552 and a scan speed of 50 nm/min. Aβ40/42 samples with a final monomeric concentration of 10 µM

553 were incubated in the absence and presence of MDK (1:2) in a similar buffer. The samples were

554 incubated at 37 ºC and studied in a time course (up to 24 h), where a stable plateau value was

555 reached. A spectrum of buffer was recorded separately and subtracted from the spectra of

556 Aβ40/42. Spectra of MDK protein were recorded separately and subtracted from the spectra of

557 Aβ and MDK, and the CD signal was given as ellipticity. Aβ (10 µM) samples incubated in absence

558 and presence of ubiquitin (1:2) were also recorded under identical conditions. Moreover, CD

559 spectra of MDK and ubiquitin were independently recorded at different time intervals and

560 subtracted from their respective buffers. For each sample, the average of five scans was recorded

561 and subsequently smoothed using Savitzky-Golay smoothing method and reported.

562

563 **Negative stain transmission electron microscopy.** Aβ species alone and reactions involving

564 Aβ together with 10 µM of MDK samples from the kinetic experiments were collected at the

565 endpoint of the ThT experiments. Additionally, Aβ samples, both in the absence and presence of

566 10 µM of ubiquitin, were collected at the endpoint of the ThT experiments. 400-mesh copper grids

567 (CF400-Cu grids, Electron Microscopy Sciences) were plasma cleaned with an Ar/O2 gas mixture

568 for 10s using Solarus plasma cleaner (Gatan), followed by 5 µl of sample. The samples were

569 allowed to absorb for 1 min before blotting away the excess liquid, followed by rinsing with Milli Q

570 water and subsequent staining using three successive applications of 2% uranyl acetate. The last

571 round of stain application was allowed to sit for 1 min before blotting away the excess stain. The

24

572   grids were air-dried prior to imaging using a 120 kV Talos L120C TEM (Thermo Fisher Scientific)

573   equipped with a CETA detector (TFS).

574

575   **Immunogold negative-stain electron microscopy.** Extraction of Aβ filaments was performed

576   as in the previous report[75]. Aβ filaments were deposited on glow-discharged 400 mesh

577   formvar/carbon coated copper grids (EM Sciences CF400-Cu) for 40 s. Subsequently, the grids

578   were blocked for 10 min with 1% BSA in PBS and incubated with anti-MDK (1:50, goat polyclonal,

579   Bio-Techne, #AF-258-SP). After rinsing with blocking buffer, the grids were incubated with anti-

580   goat IgG conjugated with 10 nm gold particle (1:20, Sigma), followed with wash and stained with

581   2% uranyl acetate for 1 min. Images were acquired at 11,000x with a Gatan Orius SC200B CCD

582   detector on a Tecnai G2 Spirit at 120 kV.

583

584   **NMR HSQC Spectroscopy.** The ^{15}N-labeled Aβ40 and Aβ42 peptides (rPeptide, #A-1101-2 and

585   #A-1102-2) were dissolved in 10 mM NaOH to a concentration of 2 mg/ml, followed by 10 min of

586   cooling and 1 min of sonication in an ice water bath. After aliquoting on ice, the samples were

587   stored in a -80°C freezer. Subsequently, 10 µM of the ^{15}N-labeled Aβ42 and Aβ40 peptides were

588   incubated with 0, 5, and 10 µM MDK in low-binding tubes (Eppendorf, #0030108434) at 37°C for

589   24 and 48 h, respectively. In addition, for control experiments Aβ42 and Aβ40, samples were

590   incubated independently in the absence and presence of ubiquitin (10 µM) at 37°C for 24 and 48

591   h, respectively. The NMR spectra of all these samples including 10 µM monomeric Aβ species,

592   were acquired on Bruker Avance 600 MHz or 800 MHz at 278K. The spectrometers are equipped

593   with a triple-resonance cryoprobe, and the data were processed in NMRPipe[76]. and analyzed

594   using NMRFAM-SPARKY[77]. The backbone resonance assignment of Aβ40 was taken from

595   BMRB (ID: 17795). Binding of MDK to the 15N-labeled Aβ40 and Aβ42 was investigated using

596   two-dimensional (2D) [^{1}H-^{15}N] so fast HMQC[78] spectrum recorded either with 32 scans or 128

25

597   scans with an interscan delay of 0.2 s. The intensity of the peaks from different spectra was

598   quantified, normalized with respect to the highest peak and used in analyzing the data.

599

600   **Preparation of Sarkosyl-soluble and -insoluble proteins from mouse brain.** The analysis

601   procedure was adapted from a previously published method[13]. Mouse cortices were lysed in a

602   low-salt buffer (50 mM HEPES, pH 7.4, 1× protease inhibitors (Thermo Fisher Scientific), 10:1

603   (v/v) ratio), and then mixed with a Sarkosyl-containing buffer (10-fold dilution) for differential

604   extraction. For ELISA analysis, a stringent buffer was used to enrich for Aβ fibrils (50 mM HEPES,

605   pH 7.4, 100 mM NaCl, 5 mM EDTA, 1.0% Triton X-100, 0.5% sodium deoxycholate, 1% Sarkosyl,

606   10% glycerol, 1× protease inhibitors). For proteomics analysis, Sarkosyl was reduced to 0.2% to

607   retain the proteins associated with Aβ fibrils. Lysates were centrifuged at 3,000 × g for 5 min to

608   remove cell debris, and the supernatant was subjected to ultracentrifugation at 55,000 rpm for 1

609   h at 4°C. The final supernatant was collected as Sarkosyl-soluble fraction, and the pellet was

610   collected and solubilized by a urea-containing buffer (50 mM HEPES, pH 8.5, 8 M urea, and 0.5%

611   sodium deoxycholate) as Sarkosyl-insoluble fraction.

612

613   **ELISA analysis.** Aβ levels in the Sarkosyl-soluble and insoluble fractions of mouse brains were

614   measured using human Aβ40 and Aβ42 ELISA kits (Invitrogen, KHB3481 and KHB3441). Briefly,

615   the strips in a 96-well plate were pre-coated with a mouse monoclonal Ab specific to the N-

616   terminus of human Aβ. Diluted protein samples (~200-fold Sarkosyl-soluble samples, and

617   ~20,000-fold Sarkosyl-insoluble samples) were added into the plate and incubated overnight at

618   4°C together with another Ab specific to the C-terminus of human Aβ40 or Aβ42. The bound

619   primary antibody was then detected using an HRP-conjugated secondary antibody, followed by a

620   1 h incubation at 21 °C. After washing, a chromogenic substrate solution was added and OD_{450}

621   was measured using a microplate reader (Epoch, BioTek).

622

623 **Immunohistochemistry.** The staining was modified from previously report[12]. Brain tissue

624 samples were fixed with 10% formalin and embedded in paraffin. 10 μm sagittal sections were

625 deparaffinized, rehydrated and rinsed with water. Antigen retrieval was performed with 10 mM

626 citric buffer (pH 6.0) with boiled water bath for 20 min and cooled down to 21 °C. Endogenous

627 peroxidase activity is further blocked by 1% H_2O_2 in PBS buffer for 10 min. After rinsed by PBS,

628 sections were then blocked with 5% donkey serum in PBS with 0.3% Triton X-100 (PBST) for 30

629 min at 21 °C followed with primary antibodies diluted with PBST plus 2% BSA and 0.2% skim milk

630 for overnight at 4°C: anti-human MDK, (goat polyclonal, 1:200, R&D, AF-258-SP), anti-mouse

631 MDK (1:200, sheep polyclonal, R&D, AF-7769), anti-Aβ (1:100, clone 82E1, IBL, 10323), anti-

632 IBA1 (1:400, rabbit polyclonal, Fujifilm Wako, 019-19741). After washing with PBS, sections were

633 then incubated with secondary antibodies (1:500, Jackson ImmunoResearch) for 1 h at 21 °C.

634 For MDK, we used HRP polymer-conjugated secondary antibodies (Vector Laboratories, MP-

635 7405), followed with signal amplification using TSA-Cy5 (1:200, Akoya Biosciences).

636 For fibrillar plaque staining, X34 dye was used due to its high specificity for binding to β-sheet

637 structures. After antigen retrieval, slides were stained with 1 mM X34 dye for 10 min, followed by

638 washes with 40% ethanol and PBS. For chromogenic immunodetection, biotin-conjugated

639 secondary antibodies were used followed with ABC reaction by Vectastain ABC kit (Vector

640 Laboratories, PK-4000) and developed by 3,3-diaminobenzidine solution (Vector Laboratories,

641 SK-4100). Images were captured by Zeiss Axioscan.Z1 and Zeiss LSM 780 confocal microscopy.

642

643 **Quantitation of Aβ plaques and microglia.** Brain tissues were serially sectioned sagittally at 10

644 μm thickness. Three slides, each representing every 30th section, were utilized for

645 immunohistochemistry followed with imaging captured with Zeiss Axioscan.Z1. QuPath, an open-

646 source software[79] was carried out for automatic quantitation of density and area of Aβ plaques

647 and microglia in an investigator blinded manner.

27

648

649   **Mass spectrometry-based proteomics.** We used an optimized protocol of TMT-LC/LC-MS/MS

650   for deep proteome profiling[48,49]. Protein samples were lysed by homogenization in the lysis buffer

651   (50 mM HEPES, pH 8.5, 8 M urea, and 0.5% sodium deoxycholate), and their concentrations

652   were measured by the BCA assay (Thermo Fisher Scientific, #23227) and confirmed by

653   Coomassie-stained short SDS gels [80]. Quantified protein samples (~0.1 mg per TMT channel)

654   were digested with Lys-C (1:100 w/w, Wako, distributor, #121-05063) for 2 h at 21 ºC, followed

655   by dilution to decrease urea to 2 M and trypsin digestion (1:50 w/w, Promega, #V5113) overnight

656   at 21 ºC. Cys residues were reduced and alkylated by iodoacetamide. The proteolysis was

657   terminated by adding trifluoroacetic acid to 1%. The resulting peptides were desalted with the

658   Sep-Pak C18 cartridges (Waters), TMT-labeled (Thermo Fisher Scientific, #A34808 and A44520),

659   and pooled equally. The pooled peptides were resolved by basic pH reverse phase LC on an

660   XBridge C18 column (3.5 µm beads, 4.6 mm x 25 cm, Waters; buffer A: 10 mM ammonium

661   formate, pH 8.0; buffer B: 95% acetonitrile, 10 mM ammonium formate, pH 8.0, ~2 h gradient, 40-

662   concatenated fractions collected)[81]. Each fraction was analyzed by acidic pH LC-MS/MS (75 µm

663   x ~20 cm, 1.9 µm C18 resin from Dr. Maisch GmbH, buffer A: 0.2% formic acid, 5% DMSO; buffer

664   B: buffer A plus 65% acetonitrile, ~1.5 h gradient). The settings of Q Exactive HF Orbitrap MS

665   (Thermo Fisher Scientific) included the MS1 scan (~410-1600 *m/z*, 60,000 resolution, 1×10^6

666   AGC and 50 ms maximal ion time) and 20 data-dependent MS2 scans (fixed first mass of 120

667   *m/z*, 60,000 resolution, 1×10^5 AGC, ~110 ms maximal ion time, HCD, 32-35% normalized

668   collision energy, ~1.0 *m/z* isolation window with 0.3 *m/z* offset, and ~15 s dynamic exclusion)[49].

669   The raw MS data were searched against protein database by the JUMP software (v1.13.4)[82],

670   which utilizes both pattern matching and *de novo* tag scoring to improve the sensitivity and

671   specificity. A composite target/decoy database was used to evaluate FDR in peptide

672   identification[83,84]. The protein target database combined downloaded Swiss-Prot, TrEMBL, and

673   UCSC databases (human: 83,955 entries; mouse: 59,423 entries). Search parameters included

674 precursor/product ion mass tolerance (± 10 ppm), full trypticity, static mass shift (TMT tags of

675 229.16293 304.2071453 and Cys carbamidomethylation of 57.02146 on cysteine), dynamic mass

676 shift (Met oxidation of 15.99492), two maximal miscleavage sites, and three maximal modification

677 sites. Peptide-spectrum matches (PSMs) were filtered by matching scores and mass accuracy to

678 limit protein FDR below 1%.

679 Proteins were quantified from TMT reporter ions based on our published method[50]. Briefly, TMT

680 reporter ion intensities were extracted for each PSM, corrected by isotopic distribution of TMT

681 reagents, filtered to remove poor PSMs (e.g., minimum intensity of 1,000), and adjusted to

682 alleviate sample pooling bias. The relative protein intensities were averaged from all assigned

683 PSMs after removing outliers (e.g., Dixon's Q-test or generalized extreme Studentized deviate

684 test). Finally, the absolute protein intensities were derived by multiplying the relative intensities

685 by the grand mean of top three abundant PSMs.

686

687 **Weighted Gene Co-expression Network Analysis (WGCNA) analysis.** The network analysis

688 was performed using WGCNA R package[51] using differentially expressed proteins. First, a signed

689 Pearson correlation matrix was computed based on the protein abundance data in all mouse

690 samples, and transformed into an adjacency matrix by applying a soft-threshold power of 16,

691 according to modified scale-free topology criterion[85]. Hierarchical clustering was then performed

692 using the dynamic tree-cutting algorithm to detect initial modules (clusters), which were

693 subsequently merged at a threshold of 0.1 (indicating high similarity on a 0 to 1 scale). Proteins

694 were ultimately assigned to the cluster with the highest correlation, with any ambiguities resolved

695 through manual curation.

696

697 **Pathway enrichment by Gene Ontology and KEGG databases.** Pathway enrichment analysis

698 was carried out by the Cluster profiler (v4.10.0)[86] to identify the biological functions of

699 dysregulated genes/proteins in a given dataset. In the analysis, we evaluated whether certain

700 biological processes or pathways were statistically overrepresented in the list of input proteins

701 compared to the background set of mouse proteome. The "enrichment" refers to the increased

702 occurrence of specific functional categories within the input list beyond what would be expected

703 by chance. The analysis was performed using Fisher's exact test against the Gene Ontology (GO)

704 biological process, molecular function, and cellular component annotations, and KEGG pathway

705 database, separately. The p values derived from Fisher's exact test were further adjusted into

706 FDR using the Benjamini-Hochberg procedure for multiple testing. Enriched pathways with FDR

707 < 10% were considered statistically significant.

708

709 **Quantitation and statistical analysis.** In small-scale analyses, two-tailed unpaired Student's

710 t-test was used for two-sample comparisons (GraphPad Prism 7.0.5). Proteomics analysis for

711 differentially expressed proteins primarily utilized the limma R package (v3.58.1)[87] in several

712 steps: (i) obtain the protein quantification data from MS as described above, (ii) perform a log

713 transformation of the data[88], (iii) calculate the p values by moderated t-test, and FDR values by

714 the Benjamini-Hochberg procedure, using limma R package, (iv) calculate the mean for each

715 protein under different conditions and derive the log2(fold change), (v) fit the log2(fold change)

716 data of all proteins to a Gaussian distribution to generate a 'global' standard deviation value.

717 Statistically significant changes were typically determined using an FDR cutoff of 5% and a log2

718 (fold change) cutoff equivalent to two standard deviations.

719

720 **Data availability**

721 The mass spectrometry proteomics data were deposited to the ProteomeXchange Consortium

722 via the PRIDE partner repository with the dataset identifiers PXD046539 and PXD061103 (the

723   whole proteome of AD mouse models), and PXD045746 and PXD061104 (the detergent-insoluble
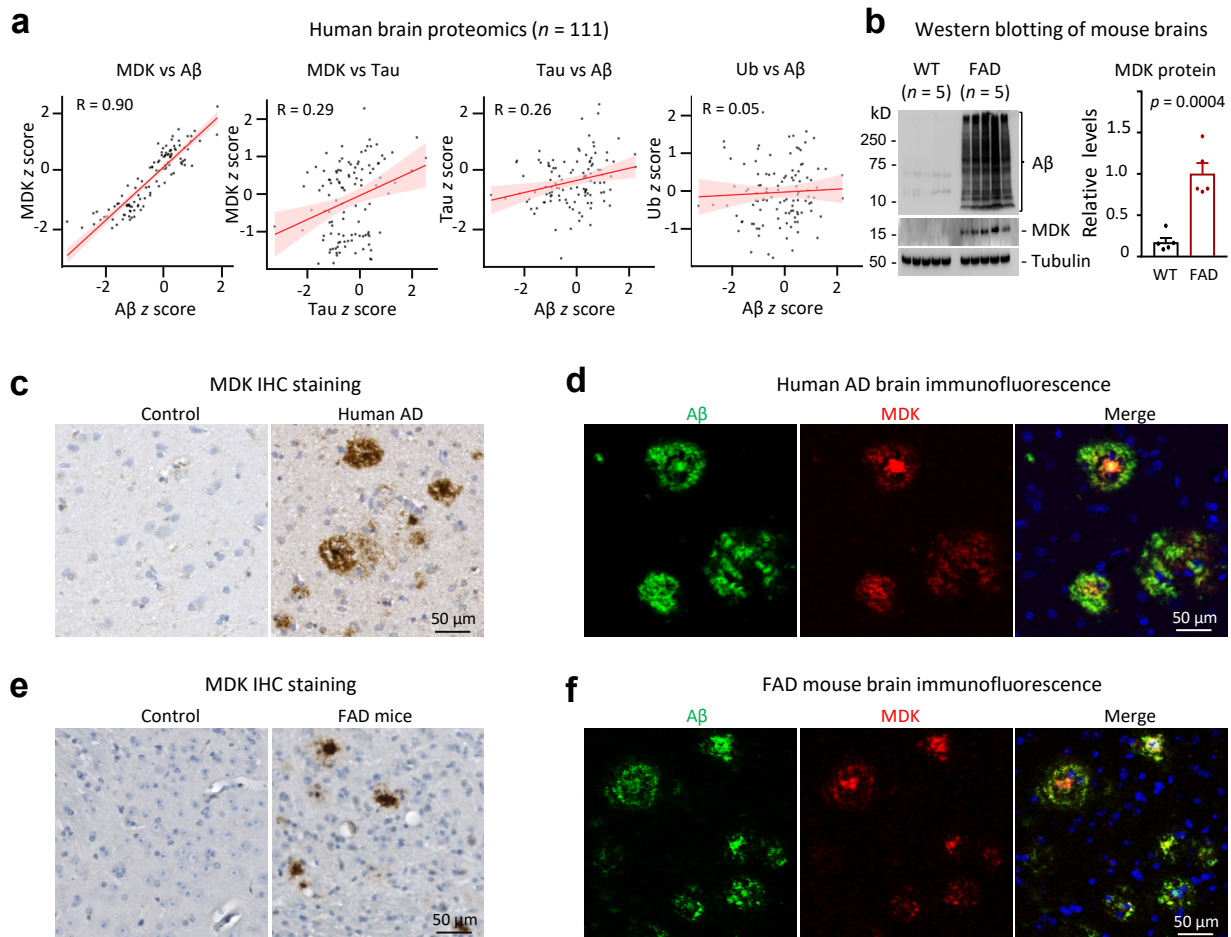
724   proteome of the mice).

725

726

Figure 1. MDK is highly correlated and colocalized with Aβ in AD and in the FAD mouse model. a, Pearson correlation analysis on MDK-Aβ, MDK-tau, tau-Aβ and Ub-Aβ levels using human brain proteomic datasets (111 cases)[16]. Protein levels were standardized to z scores. **b,** MDK level is increased in FAD mouse brains, compared to WT (12-month-old, WT n = 5, FAD n = 5). Statistical significance is analyzed by two-tailed Student's t-test. Data are shown as mean ± SEM. **c**, IHC staining of MDK in both control and AD cortical brain tissues, with the scale bar shown. **d**, Co-immunofluorescence staining of Aβ and MDK in AD cortical region, with the scale bar shown. **e**, IHC staining of MDK in WT and FAD cortical brain tissues, with the scale bar shown. **f,** Co-immunofluorescence staining of Aβ and MDK in FAD cortical region, with the scale bar shown.
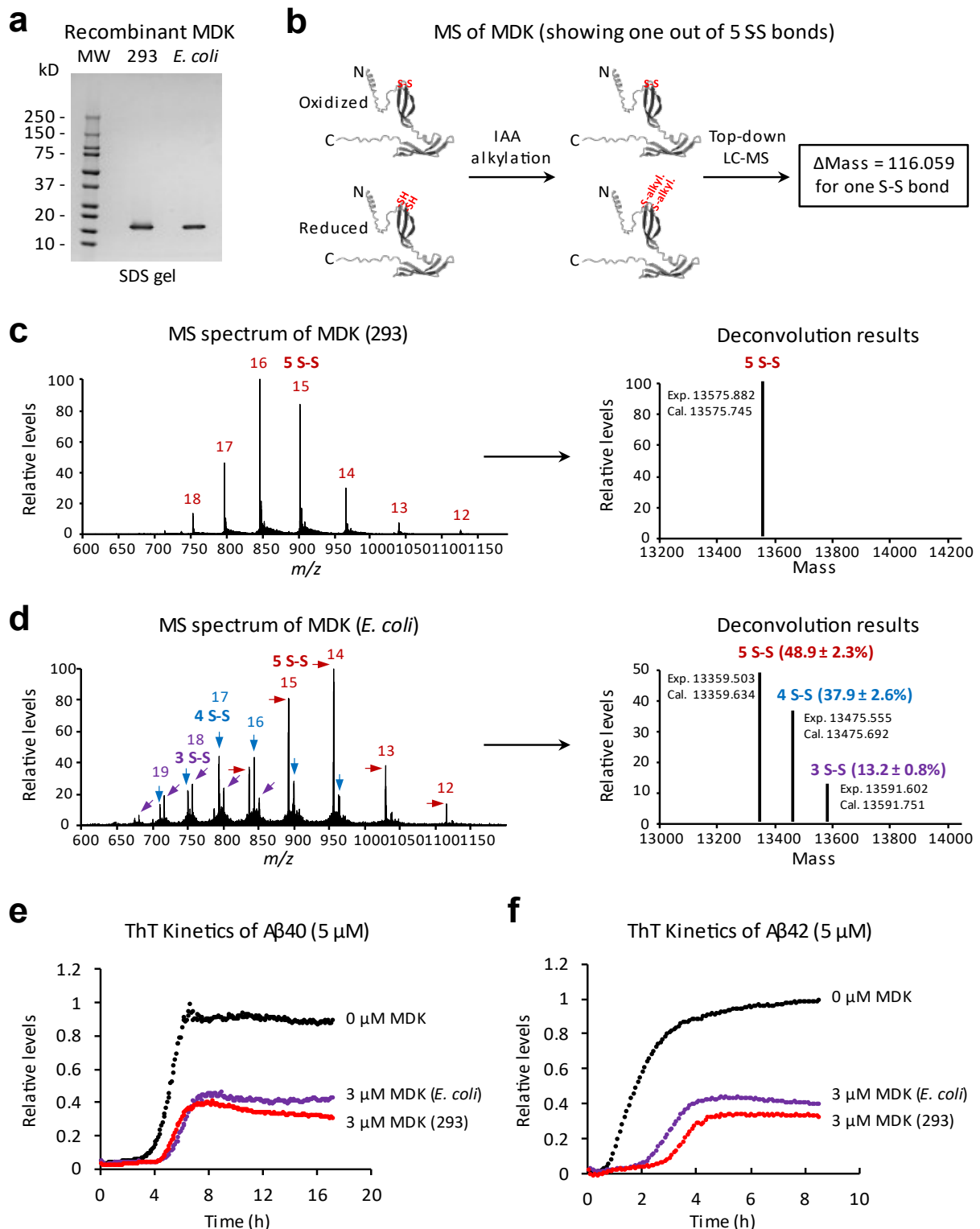
32

Figure 2. Characterization of recombinant MDK proteins and their impact on Aβ fibrillation. **a**, Highly purified recombinant MDK proteins expressed in mammalian 293 or *E. coli* cells, visualized on a stained SDS gel, with molecular weight (MW) markers. **b**, Schematic

746   representation of top-down LC-MS for analyzing disulfide bond formation in MDK proteins. Free
747   thiol (-SH) groups in Cys residues are alkylated by iodoacetamide (IAA), introducing a mass shift
748   that differentiates them from proteins with intact disulfide bonds (S-S). The AlphaFold-predicted
749   MDK structure (containing 5 S-S bonds) is downloaded, highlighting the N-terminus (N), C-
750   terminus (C) and only one S-S bond (in red). **c**, Intact mass raw spectrum and deconvoluted
751   results of 293-expressed MDK, revealing different charge states for a single protein form with 5
752   S-S bonds. **d**, Intact mass raw spectrum and deconvoluted results of *E. coli*-expressed MDK,
753   showing charge states for three protein forms containing 5, 4, or 3 S-S bonds. The relative
754   abundance of these forms was quantified from three independent scans, with data presented as
755   mean ± SEM. **e-f**, Effect of 293- or *E. coli*-expressed MDK (3 µM) on Aβ40/42 (5 µM) fibrillation
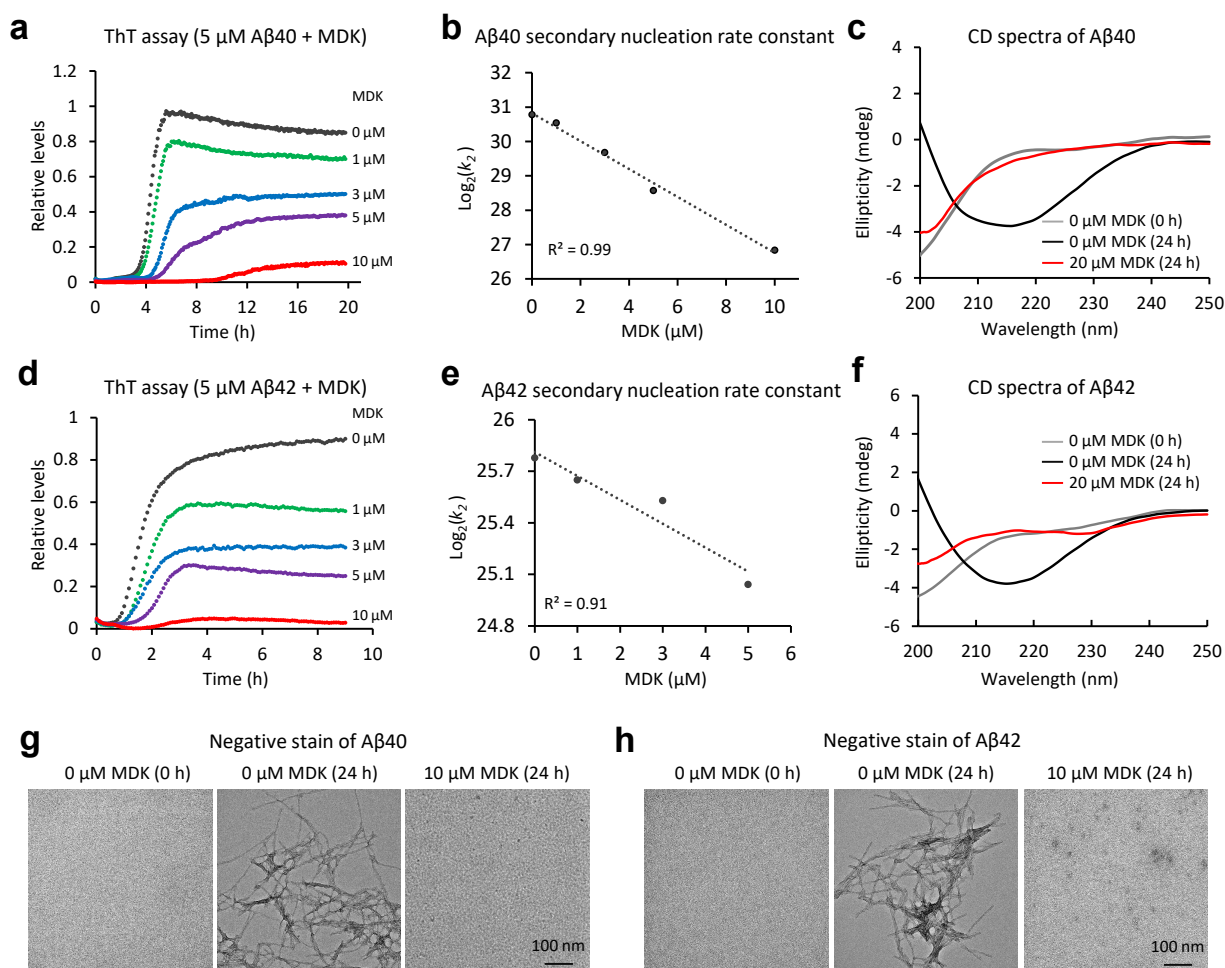756   kinetics in ThT fluorescence assays. Results represent the average of 3 replicates.
757

34

Figure 3. MDK inhibits the fibril assembly of Aβ40 and Aβ42 peptides. a, ThT fluorescence assay detecting Aβ40 amyloid fibril formation with titrated MDK protein (n = 3 replicates, averaged data shown). **b,** Analysis of secondary nucleation rate constant (k_2) by globally fitting the ThT data using AmyloFit software[35], estimating k_2 at each MDK concentration in a unit (M^{-2} h^{-1}), followed by log transformation and linear fitting of these values at different MDK concentrations. **c,** CD spectroscopy of Aβ40 (10 μM) with or without MDK, reporting ellipticity in millidegrees (mdeg). **d,** ThT assay of Aβ42 and MDK (n = 3 replicates, averaged data shown). **e,** k_2 analysis for Aβ42 fibrillation using AmyloFit. Data points from the 10 μM MDK condition did not fit well and were excluded from the fitting. **f,** CD spectroscopy of Aβ42 (10 μM) with or without MDK. **g-h,** Negative stain EM of Aβ40/MDK and Aβ42/MDK samples, respectively, with the scale bars shown.
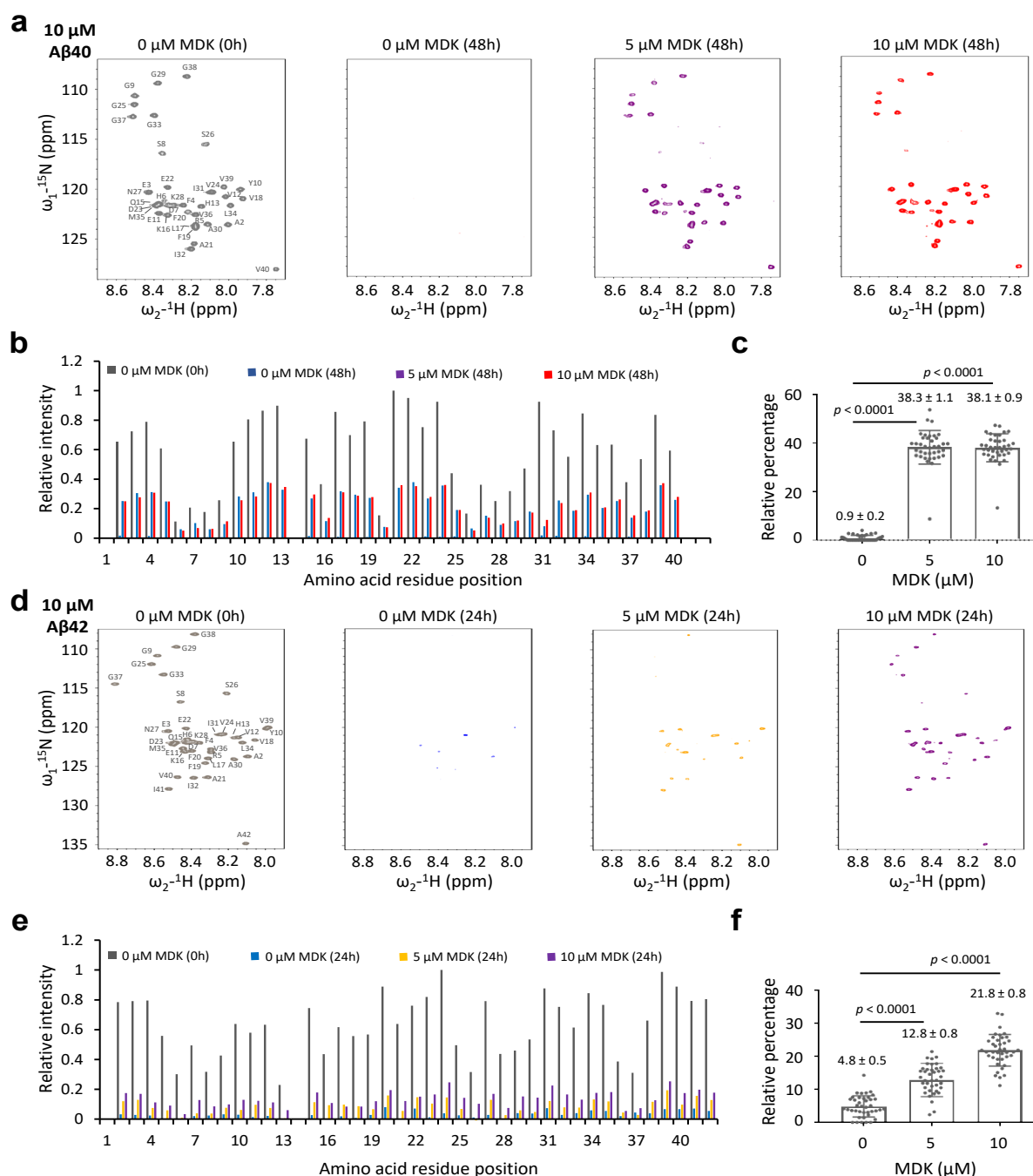
Figure 4. MDK rescues NMR signals of Aβ peptides. a, ^{1}H-^{15}N HSQC spectra of Aβ40 (10 μM) with MDK at 0, 5, or 10 μM in 50 mM Tris buffer (pH 7.5). Spectra were collected before incubation (left panel) and after 48 h incubation (right three panels). **b,** Relative cross-peak intensities for each residue, excluding D1 and H14. Intensities were normalized to a maximum value of 1. **c,** Relative percentage of Aβ40 intensities after 48 h incubation compared to pre-incubation values. Percentages were calculated pre residue and averaged, with data shown as mean ± SEM. Statistical significance was analyzed by two-tailed Student's *t*-test. **d-f,** HSQC spectra of Aβ42 under similar conditions as Aβ40, but with 24 h incubation. Statistical significance was analyzed by two-tailed Student's *t*-test.
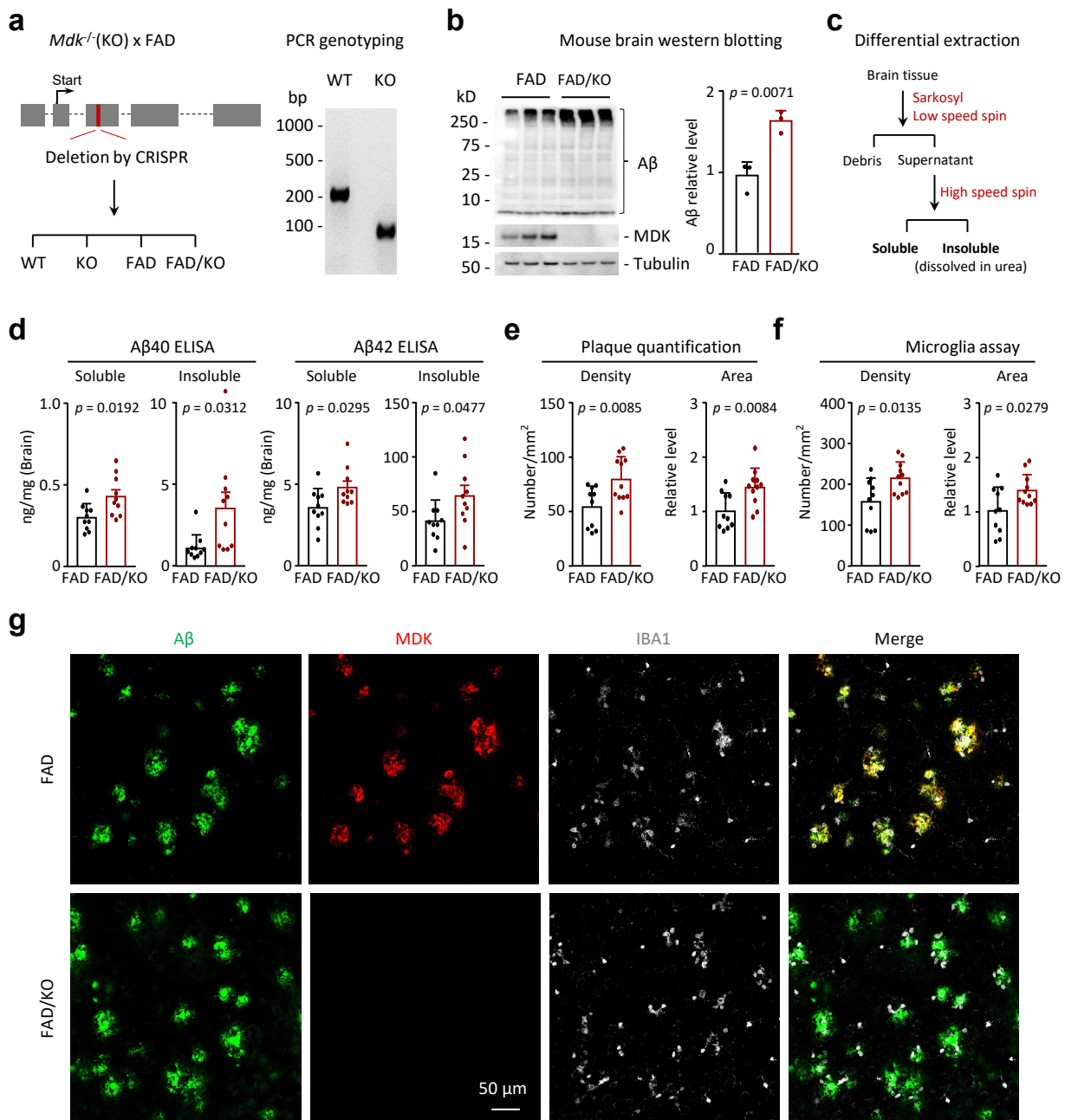
36

783

784
785

Figure 5. *Mdk* **gene knockout in FAD mice results in Aβ accumulation, plaque increase and microglia activation. a**, The diagram of the *Mdk* gene knockout and PCR genotyping of the WT and homogenous *Mdk* KO mice. The *Mdk* gene consists of five exons, including the first exon as the 5' untranslated region. A CRISPR-mediated deletion was introduced within exon 3, disrupting the open reading frame and resulting in a gene knockout. Crossbreeding of *Mdk* KO with FAD mice generated four genotypes for comparison. **b**, Western blot analysis confirming the loss of MDK protein and increased Aβ in the brain of heterogenous FAD mice with homogenous *Mdk* KO (12-month-old, *n* = 3 replicates). The Aβ intensity was quantified from the western blot image and normalized by setting the mean value of FAD mice to 1. **c**, Differential extraction to generate Sarkosyl-soluble and -insoluble fractions of mouse brains. **d**, ELISA analysis of Aβ40 and Aβ42

37

796   in the Sarkosyl-soluble and -insoluble fractions of mouse cortices (n = 10 per group), with the unit
797   of ng protein per mg brain tissue. The Sarkosyl-insoluble fractions were further dissolved in an 8
798   M urea-containing buffer and diluted for ELISA. **e**, Quantification of X34-positive amyloid plaque
799   in the cortices (FAD n = 10, FAD/KO n = 11). The relative levels of area were calculated as the
800   percentage of the total plaque area within the entire cortical region and normalized by setting the
801   mean value of FAD mice to 1. **f**, Quantification of microglia density and area in the cortices (FAD
802   n = 10, FAD/KO n = 11). **g**, Co-immunofluorescence staining of amyloid plaque, MDK and IBA1
803   in the mouse cortices. Scale bar, 50 μm. Statistical significance was analyzed using a two-tailed
804   Student's t-test if the two groups had equal variances, or by Welch's t-test if the two groups had
805   unequal variances. Data are shown as mean ± SEM. in c-f. Each point represents a data point
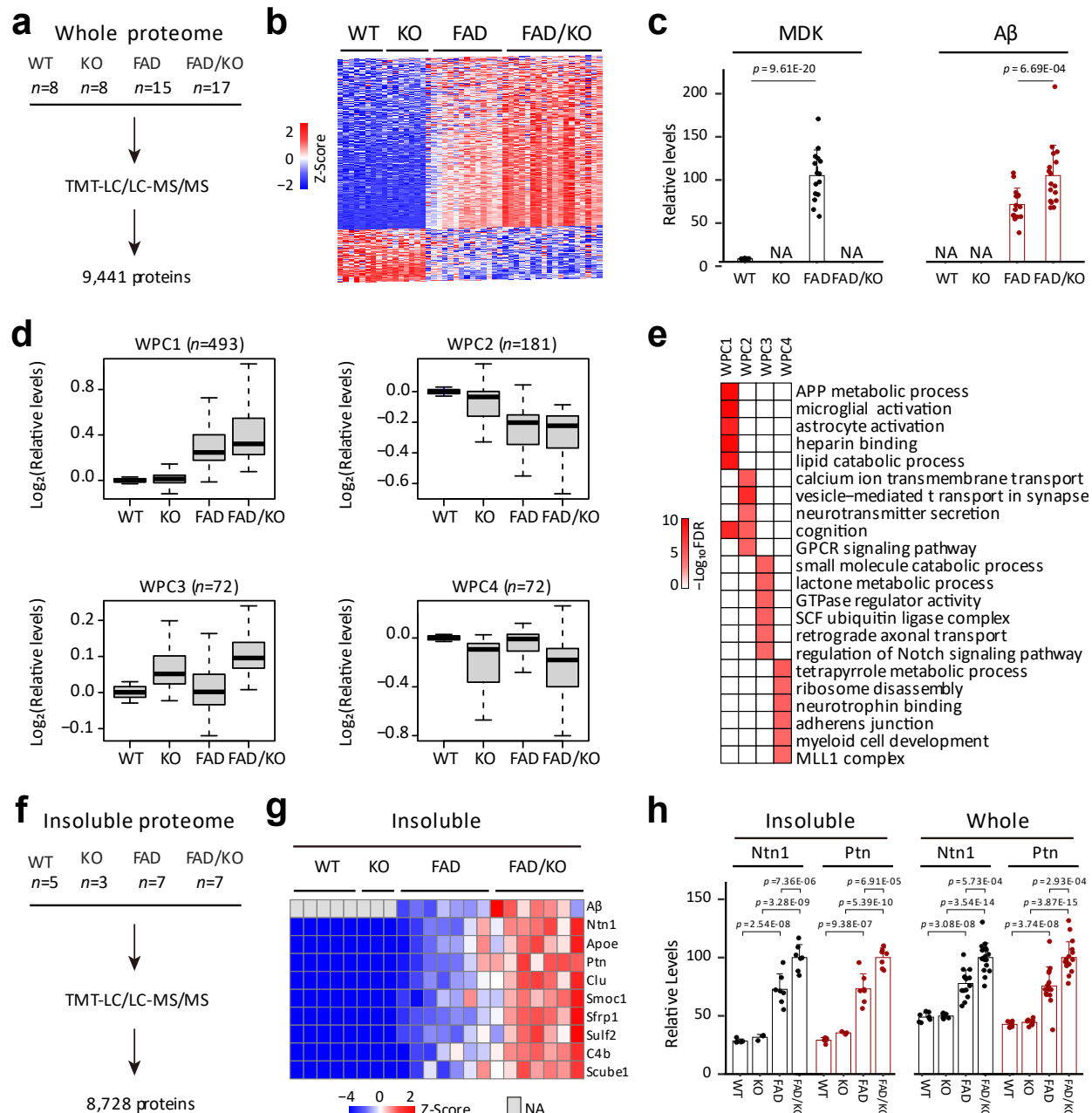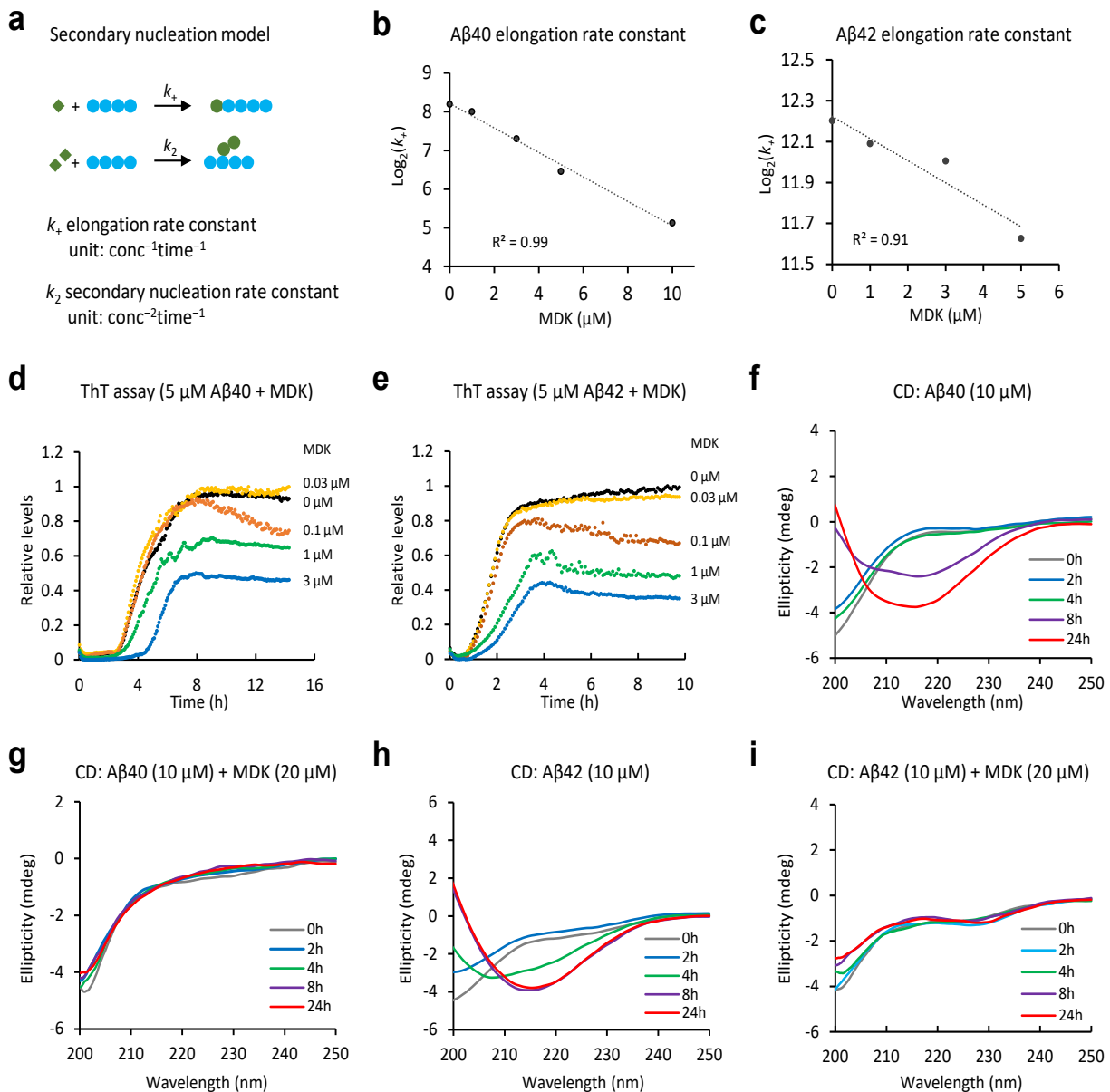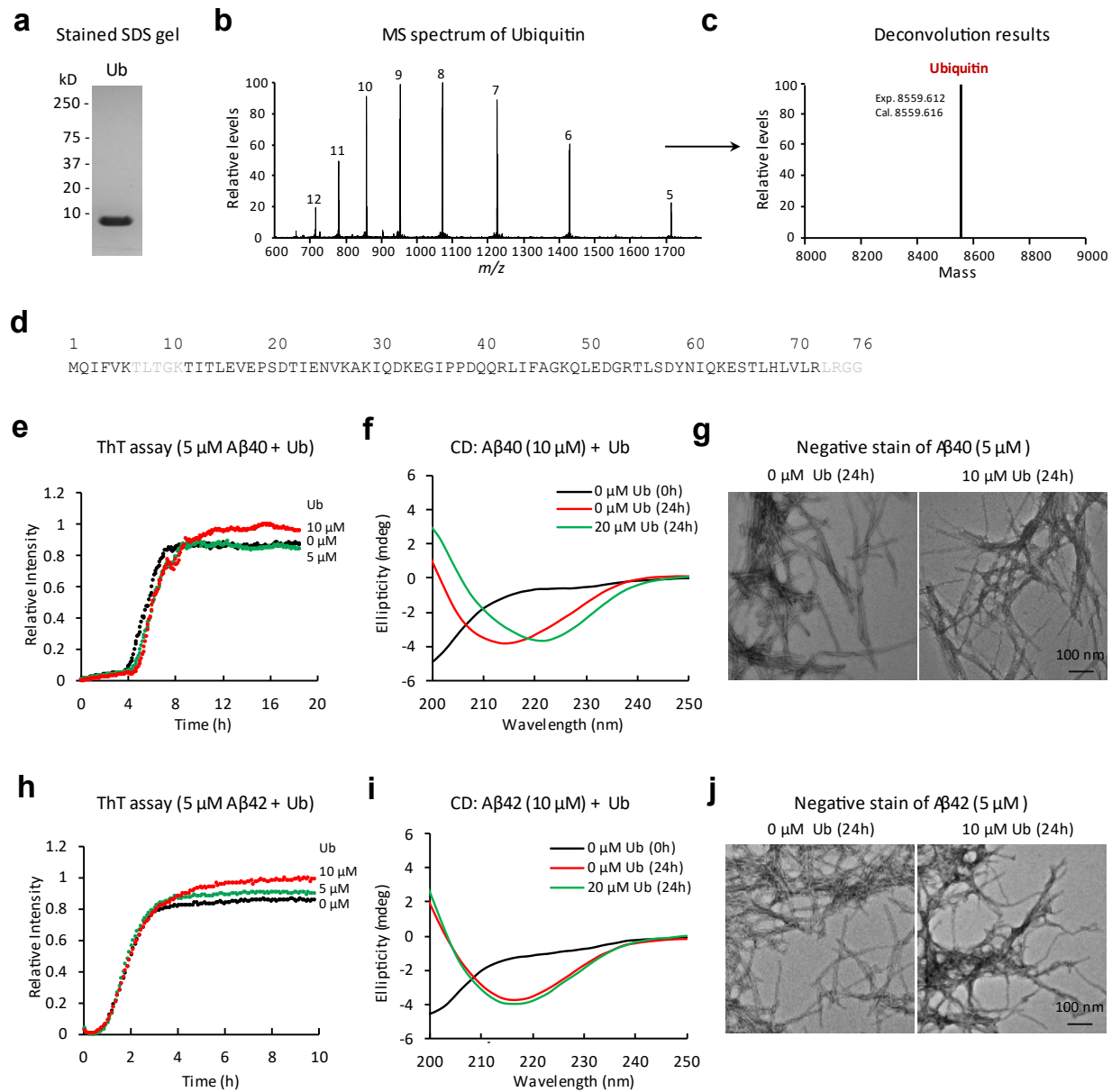806   of one mouse. Full statistical information is in Source Data Statistics.
807
808

Figure 6. Brain tissue proteomics reveals that *Mdk* knockout leads to the accumulation of Aβ and Aβ-correlated proteins, along with microglia activation in FAD. a, Workflow for whole proteome analysis of the brain cortical region from four mouse genotypes (12-month-old, WT n = 8, KO n = 8, FAD n = 15, FAD/KO n = 17). **b**, Clustering of the whole proteome using DEPs to show genotype-specific grouping. **c**, MDK and Aβ levels extracted from the whole proteome analysis. **d**, Four major DEP clusters identified by WGCNA. Protein intensities were log transformed followed by Z-score normalization. **e**, Enriched pathways in the WPC proteins, identified by Fisher's exact test. **f**, Workflow for insoluble proteome profiling (12-month-old, WT n = 5, KO n = 3, FAD n = 7, FAD/KO n = 7). **g**, Heatmap of selected proteins in the insoluble proteome, normalization by z score transformation. **h**, Ntn1 and Ptn protein levels extracted from the whole and insoluble proteome analyses. The two proteins were selected because they are highly correlated with Aβ levels in AD[16], similar to MDK (**Supplementary Data 1**). Statistical significance was determined by a two-tailed Student's t-test, with data presented as mean ± SEM.

39

a

Human MDK (293) with the cleavage site shown:

HHHHHHGSENLYFQ SSVA KKKDKVKKGGPGSECAEWAWGPCTPSSKDCGVGFREGTCGAQTQRIRCRVPCNWKKEFGADCKYKFENWGACDGGTGTKVRQGTLKKARYNAQCQETIRVTKPCTPKTKAKAKAKKGKGKD

Human MDK (*E. coli*) with the cleavage site shown:

HHHHHHSSGRENLYFQ GA KKKDKVKKGGPGSECAEWAWGPCTPSSKDCGVGFREGTCGAQTQRIRCRVPCNWKKEFGADCKYKFENWGACDGGTGTKVRQGTLKKARYNAQCQETIRVTKPCTPKTKAKAKAKKGKGKD

b

Bottom-up LC-MS/MS analysis of MDK proteins (aa 23-143)

c

d

e

Extended Data Fig. 1. Bottom-up MS analysis of recombinant MDK proteins and their effect on Aβ fibrillation. a, Protein sequences of MDK proteins expressed in mammalian 293 or *E. coli* cells. The N-terminal His-tag was cleaved after expression by TEV protease. **b,** Workflow of bottom-up LC-MS/MS analysis to characterize the positions of disulfide (S-S) bonds. Proteins were subjected to IAA alkylation, trypsin digestion and LC-MS/MS analysis. Crosslinked peptides containing single or double S-S bonds were identified. **c,** Relative peak intensities of top five crosslinked peptides (*n* = 3 replicates). **d-e,** Effect of 293- or *E. coli*-expressed MDK (10 µM) on Aβ40/42 (5 µM) fibrillation kinetics in ThT fluorescence assays. Results represent the average of 3 replicates.
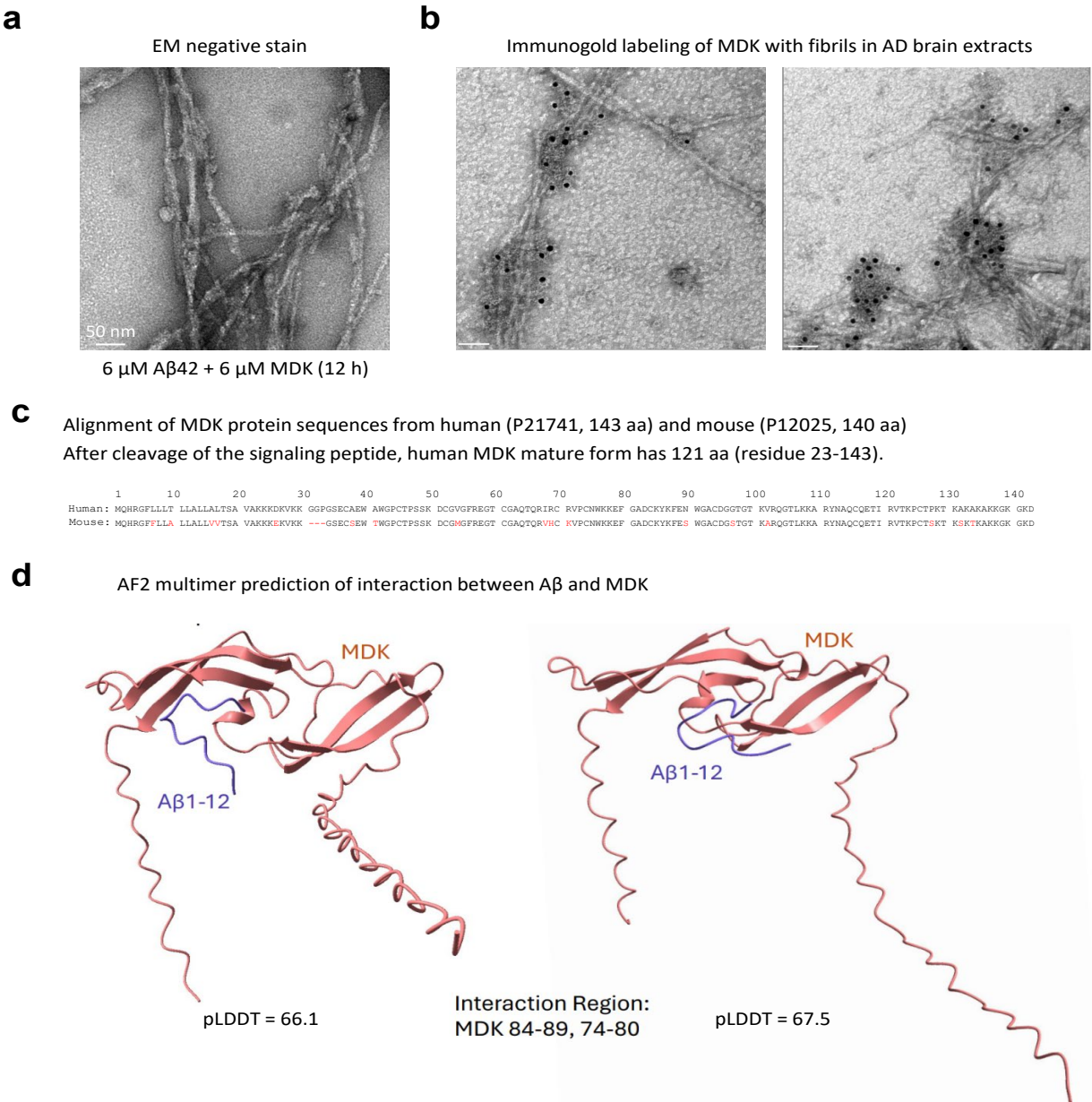
40

Extended Data Fig. 2. Characterization of the effect of MDK on Aβ fibrillation. a, Diagram of the secondary nucleation model illustrating Aβ assembly. The rate constants (k_+ and k_2) are defined with units, reflecting their dependency on protein concentration and time. **b-c,** Analysis of Aβ40 and Aβ42 elongation constants (k_+) by fitting the ThT data. **d**, Effect of MDK (0-3 μM) on Aβ40 fibrillation kinetics (n = 3 replicates, averaged data shown). **e,** Effect of MDK (0-3 μM) on Aβ42 fibrillation kinetics (n = 3 replicates, averaged data shown). **f,** Time course CD spectra of Aβ40 alone (0-24 h). **g,** Time course CD spectra of Aβ40 with MDK (0-24 h). **h,** Time course CD spectra of Aβ42 alone (0-24 h). **i,** Time course CD spectra of Aβ42 with MDK (0-24 h).

41

a Stained SDS gel

b MS spectrum of Ubiquitin

c Deconvolution results

d

```
1        10        20        30        40        50        60        70    76
MQIFVKTLTGKTITLEVEPSDTIENVKAKIQDKEGIPPDQQRLIFAGKQLEDGRTLSDYNIQKESTLHLVLRLRGG
```

e ThT assay (5 µM Aβ40 + Ub)

f CD: Aβ40 (10 µM) + Ub

g Negative stain of Aβ40 (5 µM)

h ThT assay (5 µM Aβ42 + Ub)

i CD: Aβ42 (10 µM) + Ub

j Negative stain of Aβ42 (5 µM)

848
849
850 **Extended Data Fig. 3. Characterization of ubiquitin protein by MS and its lack of effect on**
851 **Aβ40/42 fibrillation. a**, Purified Ub protein on a stained SDS gel. **b-c,** Top-down mass spectrum
852 and deconvoluted results of Ub protein showing different charge states. **d,** Bottom-up LC-MS/MS
853 analysis of Ub, covering the full Ub sequence except two short tryptic peptides (in grey). **e,** ThT
854 fluorescence assay measuring Aβ40 fibril formation at different Ub concentrations ($n = 3$
855 replicates, averaged data shown). **f**, CD spectroscopy of Aβ40 with or without Ub, with ellipticity
856 reported in millidegrees (mdeg). **g**, Negative stain EM of Aβ40/Ub samples with a scale bar (100
857 nm). **h**, ThT fluorescence assay measuring Aβ42 fibril formation at different Ub concentrations (n
858 = 3 replicates, averaged data shown). **i.** CD spectroscopy of Aβ42 with or without Ub. **j,** Negative
859 stain EM of Aβ42/Ub samples with a scale bar (100 nm).
860
861

42
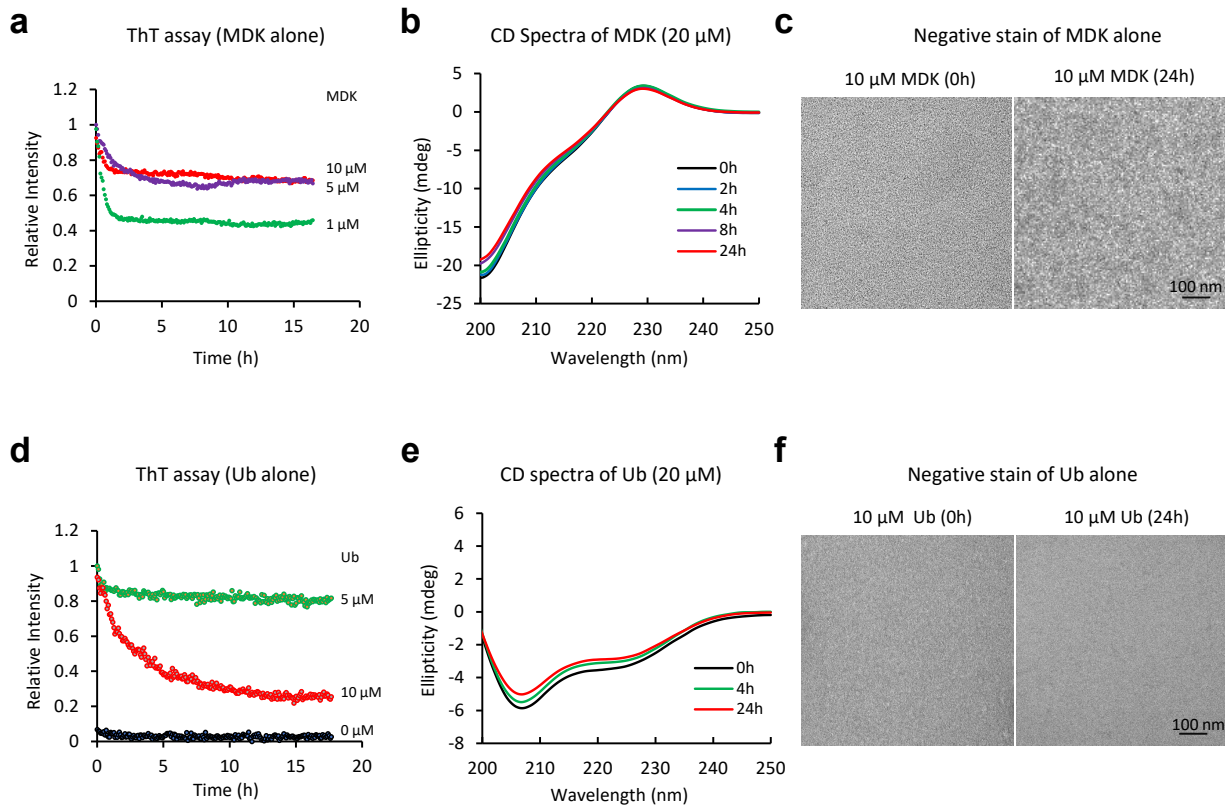
Extended Data Fig. 4. MDK or ubiquitin cannot independently assemble into fibrils. a, ThT assay of MDK alone at different concentrations (n = 3 replicates, averaged data shown). **b**, Time course CD spectra of MDK (0-24 h). **c**, Negative stain EM of the MDK samples, with a scale bar (100 nm). **d**, ThT assay of Ub alone at different concentrations (n = 3 replicates, averaged data shown). **e**, Time course CD spectra of Ub (0-24 h). **f**, Negative stain EM of the Ub samples, with a scale bar (100 nm).

872

a

EM negative stain

6 µM Aβ42 + 6 µM MDK (12 h)

b

Immunogold labeling of MDK with fibrils in AD brain extracts

c Alignment of MDK protein sequences from human (P21741, 143 aa) and mouse (P12025, 140 aa)

After cleavage of the signaling peptide, human MDK mature form has 121 aa (residue 23-143).

```
       1        10        20        30        40        50        60        70        80        90       100       110       120       130       140
Human: MQHRGFLLLT LLALLALTSA VAKKKDKVKK GGPGSECAEW AWGPCTPSSK DCGVGFREGT CGAQTQRIRC RVPCNWKKEF GADCKYKFEN WGACDGGTGT KVRQGTLKKA RYNAQCQETI RVTKPCTPKT KAKAKAKKGK GKD
Mouse: MQHRGFFLLA LLALLVVTSA VAKKKEKVKK ---GSECSEW TWGPCTPSSK DCGMGFREGT CGAQTQRVHC KVPCNWKKEF GADCKYKFES WGACDGSTGT KARQGTLKKA RYNAQCQETI RVTKPCTSKT KSKTKAKKGK GKD
```

d AF2 multimer prediction of interaction between Aβ and MDK

873
874

Extended Data Fig. 5. EM images of native Aβ filaments from patients with MDK and structural prediction of Aβ-MDK interaction. a, Negative stain EM of the fibril form of Aβ42 (6 µM) with MDK (6 µM), with scale bars (50 nm). **b**, Immunogold labeling of MDK in human brain fibrils. Enriched Aβ filaments from human AD brain lysates were analyzed with anti-MDK goat antibodies, with scale bars (50 nm). **c**, The alignment of human and mouse MDK protein sequences. MDK is a secreted protein containing a signal peptide for secretion (aa 1–22) and the main protein chain (aa 23–143). **d**, AlphaFold2-multimer predicted structures of the Aβ-MDK potential interacting interfaces. The confidence of the predicted 3D structures is evaluated by the predicted Local Distance Difference Test (pLDDT).

884
885

44
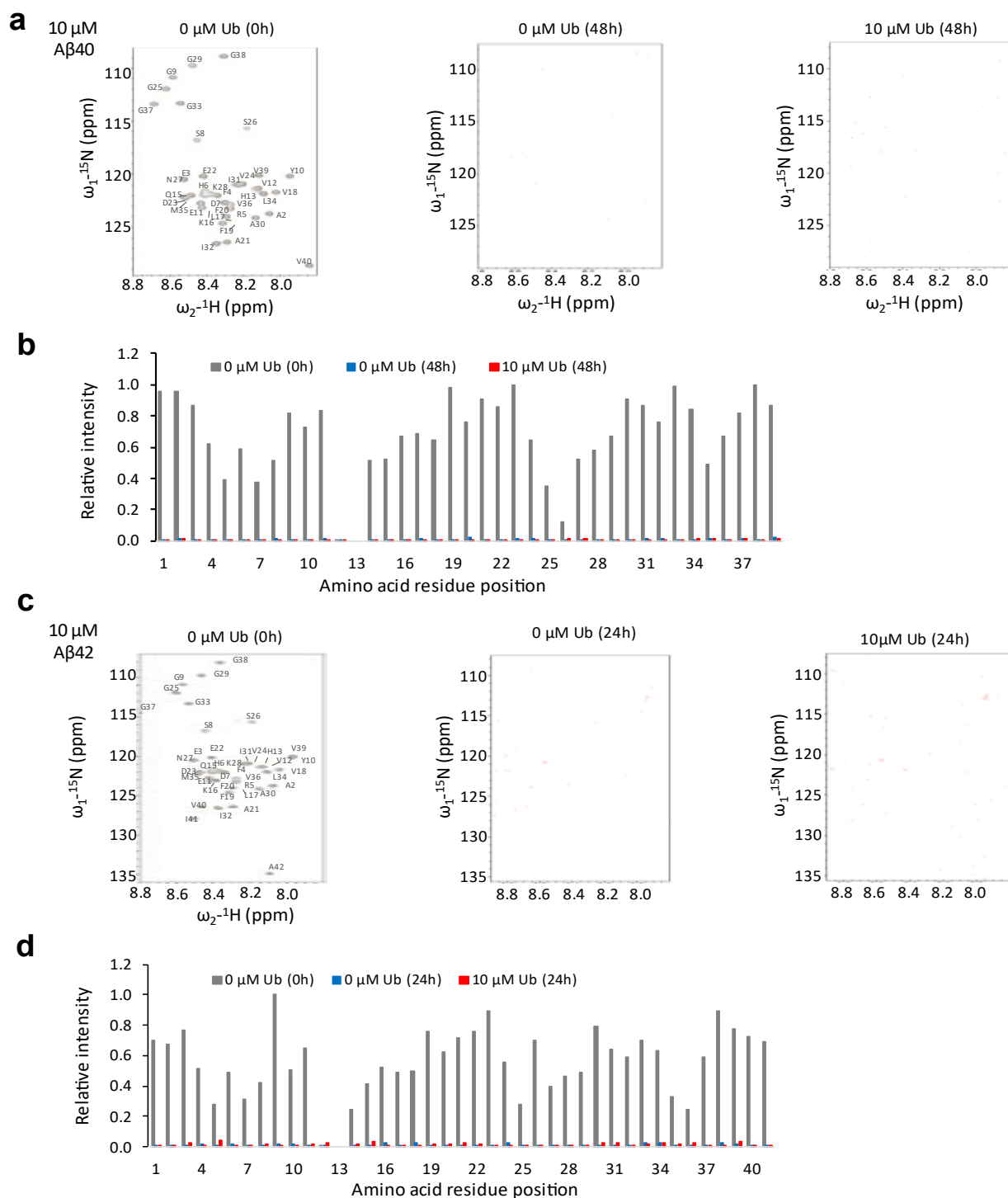
Extended Data Fig. 6. Ubiquitin cannot rescue NMR signals of Aβ peptides. a, ^{1}H-^{15}N HSQC spectra of Aβ40 (10 μM) with or without Ub (10 μM) in 50 mM Tris buffer (pH 7.5). Spectra were collected before incubation (left panel) and after 48 h incubation (right two panels). **b,** Relative cross-peak intensities for each residue, excluding D1 and H14. Intensities were normalized to a maximum value of 1. **c-d,** NMR analysis of Aβ42 under similar conditions as Aβ40, but with 24 h incubation.
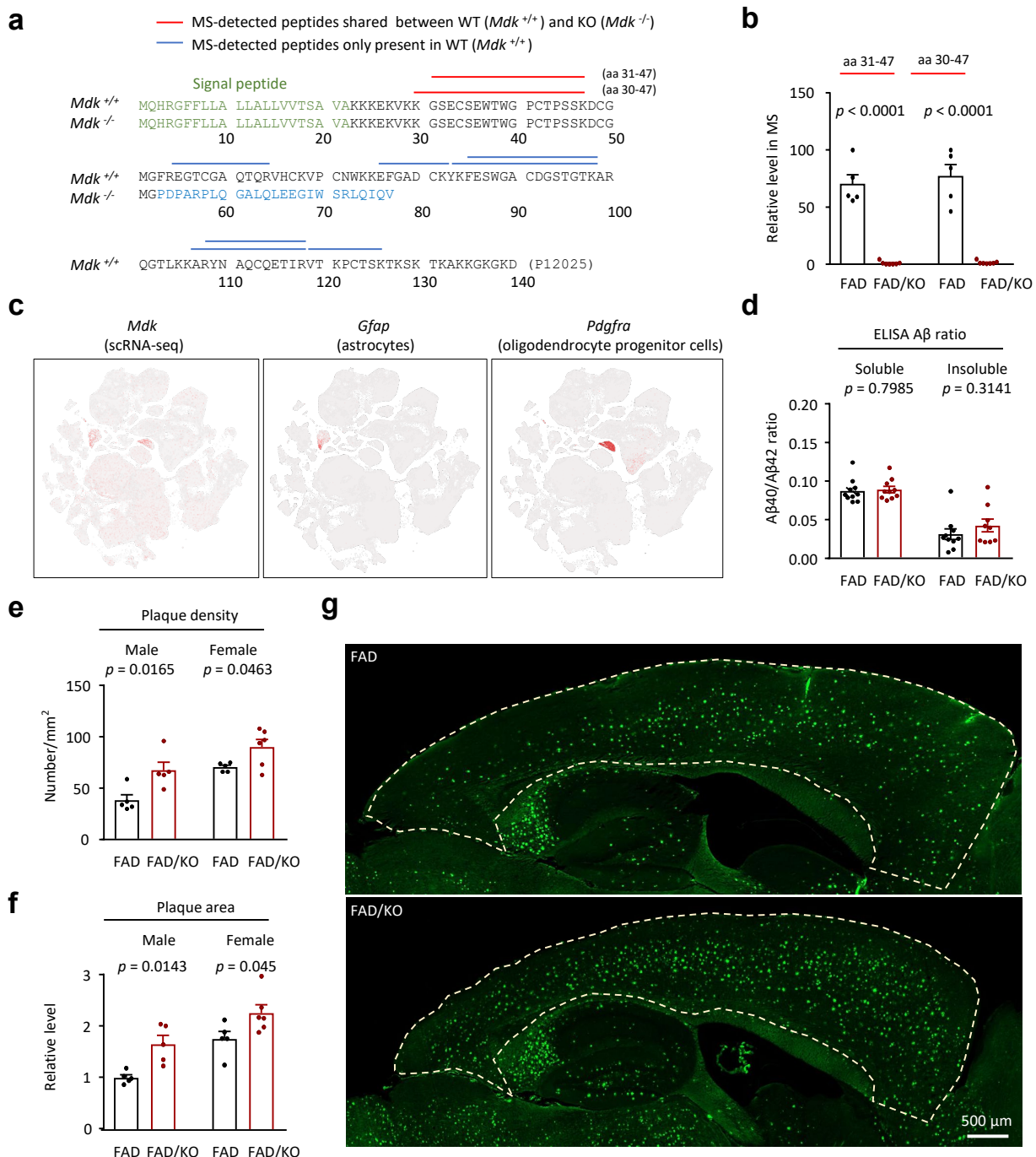
Extended Data Fig. 7. Analysis of MDK expression in KO mice, its cell-specific expression, and its impact on Aβ in male and female mice. a, Predicted mouse MDK protein sequences in WT and CRISPR-mediated KO mice, with N-terminal signal peptide shown in green. The 23 base pair deletion in MDK gene alters the open reading frame in the KO mice, potentially generating a truncated protein with distinct C-terminus (in blue) from WT. Peptides detected by MS in brain proteomic analysis are also shown, with shared peptides between MDK and the potential truncated form highlighted in red. The two peptides (aa 30-47 and aa 31-47) allow quantification of MDK full length proteins and the tentative N-terminal truncation. **b**, Quantification of two shared

46

904 peptides in FAD and FAD/KO. The intensities were normalized by setting the highest value to 100.
905 The absence of their signals in FAD/KO mice strongly suggests that the tentative N-terminal
906 truncation was not expressed at a detectable level. **c**, Expression of *Mdk*, *Gfap* (astrocyte marker)
907 and *Pdgfra* (oligodendrocyte progenitor cell marker) in mouse brain, shown in Uniform Manifold
908 Approximation and Projection (UMAP) plots. The cell-type clusters were derived from single-cell
909 RNA sequencing of more than 1.2 million cells in the whole cortex and hippocampus using the
910 10x Genomics Chromium platform[44]. Expression levels are indicated by color intensity (red). Mdk
911 is highly expressed in the 377_Astro cluster, with a trimmed mean (25-75%) $Log_2(CPM+1)$ value
912 of 4.13, as well as in the 366_Oligo cluster, with a trimmed mean value of 0.72. **d**, ELISA analysis
913 of Aβ40/Aβ42 ratio in the Sarkosyl-soluble and -insoluble fractions of mouse cortices (*n* = 10 per
914 group). **e**, Quantification of X34-positive amyloid plaque density in the cortices of male (FAD *n* =
915 5; FAD/KO *n* = 5) and female (FAD *n* = 5, FAD/KO *n* = 6). **f**, Quantification of X34-positive amyloid
916 plaque area in the cortices of the same sets of male and female mice. The results were normalized
917 by setting the mean value of FAD mice to 1. Statistical significance between FAD and FAD/KO in
918 male or female was analyzed by two-tailed Student's *t*-test. **g**, Example images of X34 staining
919 showing amyloid plaque quantification in the cortices of FAD and FAD/KO mice. Cortices were
920 outlined by the white lines. Scale bar, 500 μm. Data are shown as mean ± SEM in panels **b**, **d**, **e**,
921 **f**. Full statistical information is available in Source Data.
922
923
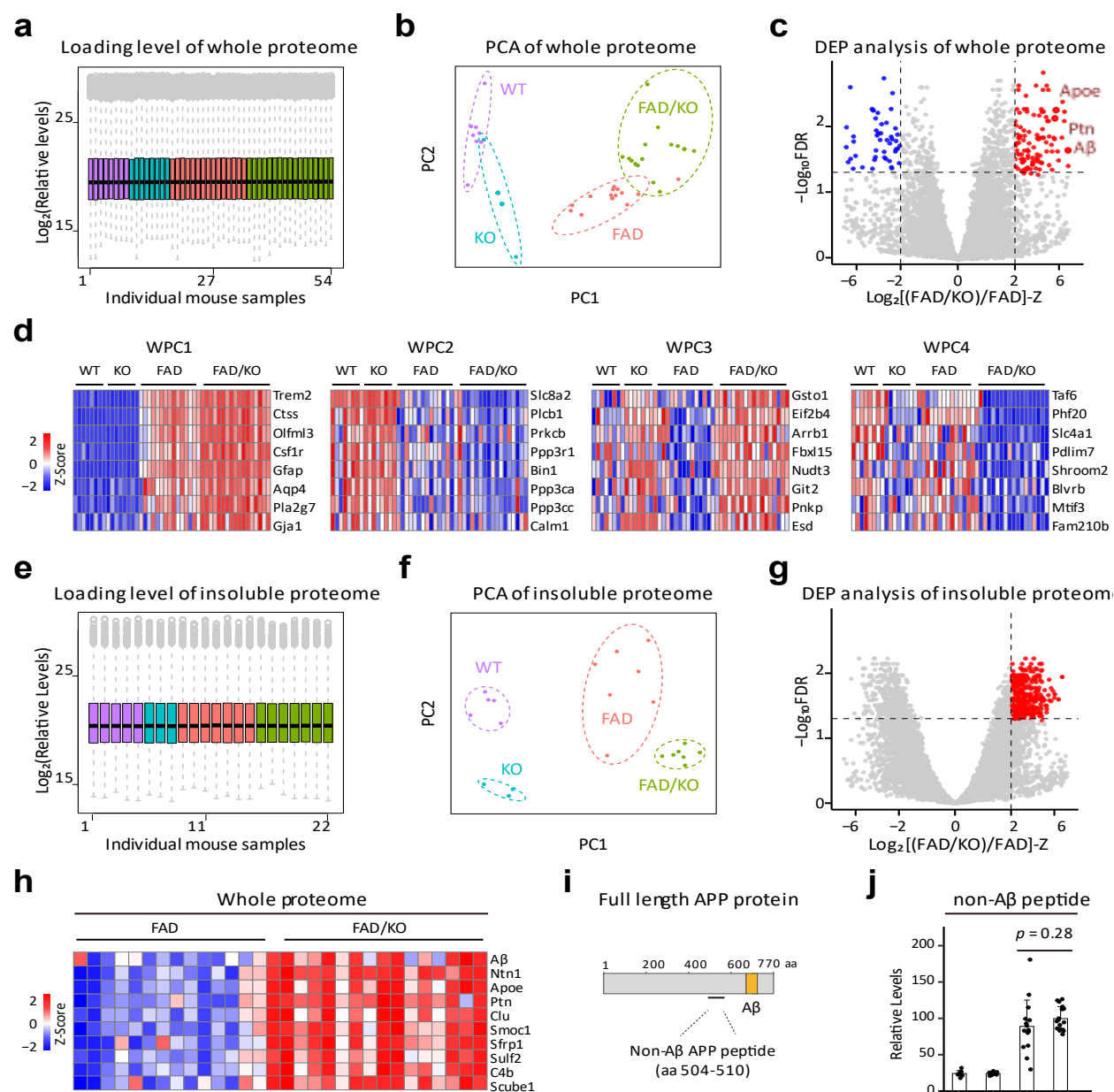
Extended Data Fig. 8. Proteomic comparison of four genotypes derived from FAD and *Mdk* KO mice. a, Boxplot of whole proteome data showing equal loading across samples, with WT, KO, FAD and FAD/KO represented in purple, blue, orange, and green, respectively. **b**, PCA of whole proteome data using DEPs, showing genotype-specific separation. **c**, Representative volcano plot showing DEPs between FAD and FAD/KO mice, with FDR values from limma analysis and log2 ratios converted to z values. **d**, Selected DEPs in four whole proteome clusters (WPC), with each protein represented by a colored box after log2 conversion and Z score analysis. **e**, Boxplot of insoluble proteome data. **f**, PCA of insoluble proteome data using DEPs. **g**, Volcano plot comparing the insoluble proteome of FAD and FAD/KO mice. **h**, Heatmap of selected DEPs shared between the insoluble and whole proteomes. **i**, Full-length APP protein diagram showing the position of a representative non-Aβ tryptic peptide. **j**, Quantification of the non-Aβ peptide levels in whole proteome across four genotypes (WT $n = 8$, KO $n = 8$, FAD $n = 15$, FAD/KO $n = 17$), with statistical significance determined by a two-tailed Student's *t*-test.

48

References

1   Alzheimer's_Association. 2023 Alzheimer's disease facts and figures. *Alzheimers Dement* **19**, 1598-1695, (2023).

2   Bellenguez, C., Grenier-Boley, B. & Lambert, J. C. Genetics of Alzheimer's disease: where we are, and where we are going. *Curr Opin Neurobiol* **61**, 40-48, (2020).

3   Bellenguez, C. *et al.* New insights into the genetic etiology of Alzheimer's disease and related dementias. *Nat Genet* **54**, 412-436, (2022).

4   Wightman, D. P. *et al.* A genome-wide association study with 1,126,563 individuals identifies new risk loci for Alzheimer's disease. *Nat Genet* **53**, 1276-1282, (2021).

5   Hardy, J. & Selkoe, D. J. The amyloid hypothesis of Alzheimer's disease: progress and problems on the road to therapeutics. *Science* **297**, 353-356, (2002).

6   Ballatore, C., Lee, V. M. & Trojanowski, J. Q. Tau-mediated neurodegeneration in Alzheimer's disease and related disorders. *Nat Rev Neurosci* **8**, 663-672, (2007).

7   Neumann, M. *et al.* Ubiquitinated TDP-43 in frontotemporal lobar degeneration and amyotrophic lateral sclerosis. *Science* **314**, 130-133, (2006).

8   Nelson, P. T. *et al.* Limbic-predominant age-related TDP-43 encephalopathy (LATE): consensus working group report. *Brain* **142**, 1503-1527, (2019).

9   Bai, B. *et al.* U1 small nuclear ribonucleoprotein complex and RNA splicing alterations in Alzheimer's disease. *Proc Natl Acad Sci U S A* **110**, 16562-16567, (2013).

10   Bai, B. *et al.* Integrated Approaches for Analyzing U1-70K Cleavage in Alzheimer's Disease. *J Proteome Res* **13**, 4526-4534, (2014).

11   Hales, C. M. *et al.* U1 small nuclear ribonucleoproteins (snRNPs) aggregate in Alzheimer's disease due to autosomal dominant genetic mutations and trisomy 21. *Mol Neurodegener* **9**, 15, (2014).

12   Chen, P. C. *et al.* Alzheimer's disease-associated U1 snRNP splicing dysfunction causes neuronal hyperexcitability and cognitive impairment. *Nat Aging* **2**, 923-940, (2022).

13   Zaman, M. *et al.* Dissecting Detergent-Insoluble Proteome in Alzheimer's Disease by TMTc-Corrected Quantitative Mass Spectrometry. *Mol Cell Proteomics* **22**, 100608, (2023).

14   van Dyck, C. H. *et al.* Lecanemab in Early Alzheimer's Disease. *N Engl J Med* **388**, 9-21, (2023).

15   Sims, J. R. *et al.* Donanemab in Early Symptomatic Alzheimer Disease: The TRAILBLAZER-ALZ 2 Randomized Clinical Trial. *JAMA* **330**, 512-527, (2023).

16   Bai, B. *et al.* Deep Multilayer Brain Proteomics Identifies Molecular Networks in Alzheimer's Disease Progression. *Neuron* **105**, 975-991, (2020).

17   Wang, H. *et al.* Integrated analysis of ultra-deep proteomes in cortex, cerebrospinal fluid and serum reveals a mitochondrial signature in Alzheimer's disease. *Mol Neurodegener* **15**, 43, (2020).

18   Higginbotham, L. *et al.* Integrated proteomics reveals brain-based cerebrospinal fluid biomarkers in asymptomatic and symptomatic Alzheimer's disease. *Sci Adv* **6**, eaaz9360, (2020).

19   Johnson, E. C. B. *et al.* Large-scale deep multi-layer analysis of Alzheimer's disease brain reveals strong proteomic disease-related changes not observed at the RNA level. *Nat Neurosci* **25**, 213-225, (2022).

20   Sathe, G. *et al.* Quantitative proteomic analysis of the frontal cortex in Alzheimer's disease. *J Neurochem* **156**, 988-1002, (2021).

21   Roberts, J. A. *et al.* A brain proteomic signature of incipient Alzheimer's disease in young APOE epsilon4 carriers identifies novel drug targets. *Sci Adv* **7**, eabi8178, (2021).

987   22   Bai, B. *et al.* Proteomic landscape of Alzheimer's disease: novel insights into pathogenesis
988   and biomarker discovery. *Mol Neurodegener* **16**, 55, (2021).
989   23   Askenazi, M. *et al.* Compilation of reported protein changes in the brain in Alzheimer's
990   disease. *Nat Commun* **14**, 4466, (2023).
991   24   Yarbro, J. M. *et al.* Human and mouse proteomics reveals the shared pathways in
992   Alzheimer's disease and delayed protein turnover in the amyloidome. *Nat Commun* **16**,
993   1533, (2025).
994   25   Li, W. *et al.* An Extensive Atlas of Proteome and Phosphoproteome Turnover Across
995   Mouse Tissues and Brain Regions. *bioRxiv*, (2024).
996   26   Liao, L. *et al.* Proteomic characterization of postmortem amyloid plaques isolated by laser
997   capture microdissection. *J. Biol. Chem.* **279**, 37061-37068, (2004).
998   27   Xiong, F., Ge, W. & Ma, C. Quantitative proteomics reveals distinct composition of amyloid
999   plaques in Alzheimer's disease. *Alzheimers Dement* **15**, 429-440, (2019).
1000 28   Drummond, E. *et al.* The amyloid plaque proteome in early onset Alzheimer's disease and
1001   Down syndrome. *Acta Neuropathol Commun* **10**, 53, (2022).
1002 29   Rahman, M. M. & Lendel, C. Extracellular protein components of amyloid plaques and
1003   their roles in Alzheimer's disease pathology. *Mol Neurodegener* **16**, 59, (2021).
1004 30   Ross-Munro, E. *et al.* Midkine: The Who, What, Where, and When of a Promising
1005   Neurotrophic Therapy for Perinatal Brain Injury. *Front Neurol* **11**, 568814, (2020).
1006 31   Yasuhara, O. *et al.* Midkine, a novel neurotrophic factor, is present in senile plaques of
1007   Alzheimer disease. *Biochem Biophys Res Commun* **192**, 246-251, (1993).
1008 32   Muramatsu, H. *et al.* Midkine as a factor to counteract the deposition of amyloid beta-
1009   peptide plaques: in vitro analysis and examination in knockout mice. *Int Arch Med* **4**, 1,
1010   (2011).
1011 33   Oakley, H. *et al.* Intraneuronal beta-amyloid aggregates, neurodegeneration, and neuron
1012   loss in transgenic mice with five familial Alzheimer's disease mutations: potential factors
1013   in amyloid plaque formation. *J Neurosci* **26**, 10129-10140, (2006).
1014 34   LeVine, H., 3rd. Thioflavine T interaction with synthetic Alzheimer's disease beta-amyloid
1015   peptides: detection of amyloid aggregation in solution. *Protein Sci* **2**, 404-410, (1993).
1016 35   Meisl, G. *et al.* Molecular mechanisms of protein aggregation from global fitting of kinetic
1017   models. *Nat Protoc* **11**, 252-272, (2016).
1018 36   Yang, Y. *et al.* Cryo-EM structures of amyloid-beta 42 filaments from human brains.
1019   *Science* **375**, 167-172, (2022).
1020 37   Kollmer, M. *et al.* Cryo-EM structure and polymorphism of Abeta amyloid fibrils purified
1021   from Alzheimer's brain tissue. *Nat Commun* **10**, 4760, (2019).
1022 38   Lu, J. X. *et al.* Molecular structure of beta-amyloid fibrils in Alzheimer's disease brain
1023   tissue. *Cell* **154**, 1257-1268, (2013).
1024 39   Sawaya, M. R., Hughes, M. P., Rodriguez, J. A., Riek, R. & Eisenberg, D. S. The
1025   expanding amyloid family: Structure, stability, function, and pathogenesis. *Cell* **184**, 4857-
1026   4873, (2021).
1027 40   Yang, Y. *et al.* Cryo-EM structures of amyloid-beta filaments with the Arctic mutation
1028   (E22G) from human and mouse brains. *Acta Neuropathol* **145**, 325-333, (2023).
1029 41   Evans, R., O'Neill, M., Pritzel, A., Antropova, N., Senior, A., Green, T., ... & Hassabis, D.
1030   . Protein complex prediction with AlphaFold-Multimer. *biorxiv*, DOI:
1031   10.1101/2021.1110.1104.463034, (2022).
1032 42   Roche, J., Shen, Y., Lee, J. H., Ying, J. & Bax, A. Monomeric Aβ(1-40) and Aβ(1-42)
1033   Peptides in Solution Adopt Very Similar Ramachandran Map Distributions That Closely
1034   Resemble Random Coil. *Biochemistry* **55**, 762-775, (2016).
1035 43   Wallin, C. *et al.* The Neuronal Tau Protein Blocks in Vitro Fibrillation of the Amyloid-β (Aβ)
1036   Peptide at the Oligomeric Stage. *J Am Chem Soc* **140**, 8138-8146, (2018).

1037 44   Yao, Z. *et al.* A transcriptomic and epigenomic cell atlas of the mouse primary motor
1038   cortex. *Nature* **598**, 103-110, (2021).
1039 45   Styren, S. D., Hamilton, R. L., Styren, G. C. & Klunk, W. E. X-34, a fluorescent derivative
1040   of Congo red: a novel histochemical stain for Alzheimer's disease pathology. *J Histochem*
1041   *Cytochem* **48**, 1223-1232, (2000).
1042 46   Ito, D. *et al.* Microglia-specific localisation of a novel calcium binding protein, Iba1. *Brain*
1043   *Res Mol Brain Res* **57**, 1-9, (1998).
1044 47   Schwabenland, M. *et al.* Analyzing microglial phenotypes across neuropathologies: a
1045   practical guide. *Acta Neuropathol* **142**, 923-936, (2021).
1046 48   Bai, B. *et al.* Deep Profiling of Proteome and Phosphoproteome by Isobaric Labeling,
1047   Extensive Liquid Chromatography, and Mass Spectrometry. *Methods Enzymol* **585**, 377-
1048   395, (2017).
1049 49   Wang, Z. *et al.* 27-plex Tandem Mass Tag Mass Spectrometry for Profiling Brain Proteome
1050   in Alzheimer's Disease. *Anal Chem* **92**, 7162-7170, (2020).
1051 50   Niu, M. *et al.* Extensive Peptide Fractionation and y1 Ion-Based Interference Detection
1052   Method for Enabling Accurate Quantification by Isobaric Labeling and Mass Spectrometry.
1053   *Anal Chem* **89**, 2956-2963, (2017).
1054 51   Langfelder, P. & Horvath, S. WGCNA: an R package for weighted correlation network
1055   analysis. *BMC Bioinformatics* **9**, 559, (2008).
1056 52   Sousa, C. *et al.* Single-cell transcriptomics reveals distinct inflammation-induced microglia
1057   signatures. *EMBO Rep* **19**, (2018).
1058 53   Zhang, Y. *et al.* Purification and Characterization of Progenitor and Mature Human
1059   Astrocytes Reveals Transcriptional and Functional Differences with Mouse. *Neuron* **89**,
1060   37-53, (2016).
1061 54   Saha, O. *et al.* The Alzheimer's disease risk gene BIN1 regulates activity-dependent gene
1062   expression in human-induced glutamatergic neurons. *Molecular psychiatry*, (2024).
1063 55   Voskobiynyk, Y. *et al.* Alzheimer's disease risk gene BIN1 induces Tau-dependent
1064   network hyperexcitability. *Elife* **9**, (2020).
1065 56   Arvidsson, U., Riedl, M., Elde, R. & Meister, B. Vesicular acetylcholine transporter
1066   (VAChT) protein: a novel and unique marker for cholinergic neurons in the central and
1067   peripheral nervous systems. *J Comp Neurol* **378**, 454-467, (1997).
1068 57   Rasmussen, N. L., Kournoutis, A., Lamark, T. & Johansen, T. NBR1: The archetypal
1069   selective autophagy receptor. *J Cell Biol* **221**, (2022).
1070 58   Cohen, S. I. *et al.* Proliferation of amyloid-β42 aggregates occurs through a secondary
1071   nucleation mechanism. *Proc Natl Acad Sci U S A* **110**, 9758-9763, (2013).
1072 59   Lee, J., Culyba, E. K., Powers, E. T. & Kelly, J. W. Amyloid-β forms fibrils by nucleated
1073   conformational conversion of oligomers. *Nature chemical biology* **7**, 602-609, (2011).
1074 60   Belsare, K. D. *et al.* Soluble TREM2 inhibits secondary nucleation of Aβ fibrillization and
1075   enhances cellular uptake of fibrillar Aβ. *Proc Natl Acad Sci U S A* **119**, (2022).
1076 61   Gao, Y., Schedin-Weiss, S. & Tjernberg, L. O. A closer look at pathogenic amyloid-β in
1077   Alzheimer's disease using cryo-electron microscopy: a narrative review. *Advanced*
1078   *Technology in Neuroscience* **1**, 177-187, (2024).
1079 62   Maeda, N. *et al.* A receptor-like protein-tyrosine phosphatase PTPzeta/RPTPbeta binds a
1080   heparin-binding growth factor midkine. Involvement of arginine 78 of midkine in the high
1081   affinity binding to PTPzeta. *J Biol Chem* **274**, 12474-12479, (1999).
1082 63   Muramatsu, H. *et al.* LDL receptor-related protein as a component of the midkine receptor.
1083   *Biochem Biophys Res Commun* **270**, 936-941, (2000).
1084 64   Muramatsu, H. *et al.* alpha4beta1- and alpha6beta1-integrins are functional receptors for
1085   midkine, a heparin-binding growth factor. *J Cell Sci* **117**, 5405-5415, (2004).

51

65   Ichihara-Tanaka, K., Oohira, A., Rumsby, M. & Muramatsu, T. Neuroglycan C is a novel midkine receptor involved in process elongation of oligodendroglial precursor-like cells. *J Biol Chem* **281**, 30857-30864, (2006).

66   Stoica, G. E. *et al.* Midkine binds to anaplastic lymphoma kinase (ALK) and acts as a growth factor for different cell types. *J Biol Chem* **277**, 35990-35998, (2002).

67   Huang, Y. *et al.* Midkine induces epithelial-mesenchymal transition through Notch2/Jak2-Stat3 signaling in human keratinocytes. *Cell Cycle* **7**, 1613-1622, (2008).

68   Yamazaki, Y., Zhao, N., Caulfield, T. R., Liu, C. C. & Bu, G. Apolipoprotein E and Alzheimer disease: pathobiology and targeting strategies. *Nat Rev Neurol* **15**, 501-518, (2019).

69   Levites, Y. *et al.* Integrative proteomics identifies a conserved Abeta amyloid responsome, novel plaque proteins, and pathology modifiers in Alzheimer's disease. *Cell Rep Med* **5**, 101669, (2024).

70   Chishti, M. A. *et al.* Early-onset amyloid deposition and cognitive deficits in transgenic mice expressing a double mutant form of amyloid precursor protein 695. *J Biol Chem* **276**, 21562-21570, (2001).

71   Beach, T. G. *et al.* Arizona Study of Aging and Neurodegenerative Disorders and Brain and Body Donation Program. *Neuropathology* **35**, 354-389, (2015).

72   Connelly, J. P. & Pruett-Miller, S. M. CRIS.py: A Versatile and High-throughput Analysis Program for CRISPR-based Genome Editing. *Sci Rep* **9**, 4194, (2019).

73   Narina, S., Connelly, J. P. & Pruett-Miller, S. M. High-Throughput Analysis of CRISPR-Cas9 Editing Outcomes in Cell and Animal Models Using CRIS.py. *Methods Mol Biol* **2631**, 155-182, (2023).

74   Chen, Z. L. *et al.* A high-speed search engine pLink 2 with systematic evaluation for proteome-scale identification of cross-linked peptides. *Nat Commun* **10**, 3404, (2019).

75   Yang, Y. *et al.* Cryo-EM structures of amyloid-β 42 filaments from human brains. *Science* **375**, 167-172, (2022).

76   Delaglio, F. *et al.* NMRPipe: a multidimensional spectral processing system based on UNIX pipes. *J Biomol NMR* **6**, 277-293, (1995).

77   Lee, W., Tonelli, M. & Markley, J. L. NMRFAM-SPARKY: enhanced software for biomolecular NMR spectroscopy. *Bioinformatics* **31**, 1325-1327, (2015).

78   Schanda, P., Kupce, E. & Brutscher, B. SOFAST-HMQC experiments for recording two-dimensional heteronuclear correlation spectra of proteins within a few seconds. *J Biomol NMR* **33**, 199-211, (2005).

79   Bankhead, P. *et al.* QuPath: Open source software for digital pathology image analysis. *Sci Rep* **7**, 16878, (2017).

80   Xu, P., Duong, D. M. & Peng, J. Systematical Optimization of Reverse-Phase Chromatography for Shotgun Proteomics. *J Proteome Res* **8**, 3944-3950, (2009).

81   Wang, H. *et al.* Systematic optimization of long gradient chromatography mass spectrometry for deep analysis of brain proteome. *J Proteome Res* **14**, 829-838, (2015).

82   Wang, X. *et al.* JUMP: a tag-based database search tool for peptide identification with high sensitivity and accuracy. *Mol Cell Proteomics* **13**, 3663-3673, (2014).

83   Peng, J., Elias, J. E., Thoreen, C. C., Licklider, L. J. & Gygi, S. P. Evaluation of multidimensional chromatography coupled with tandem mass spectrometry (LC/LC-MS/MS) for large-scale protein analysis: the yeast proteome. *J Proteome Res* **2**, 43-50, (2003).

84   Elias, J. E. & Gygi, S. P. Target-decoy search strategy for increased confidence in large-scale protein identifications by mass spectrometry. *Nat Methods* **4**, 207-214, (2007).

85   Zhang, B. & Horvath, S. A general framework for weighted gene co-expression network analysis. *Stat Appl Genet Mol Biol* **4**, Article17, (2005).

1136 86   Yu, G., Wang, L. G., Han, Y. & He, Q. Y. clusterProfiler: an R package for comparing
1137   biological themes among gene clusters. *OMICS* **16**, 284-287, (2012).
1138 87   Ritchie, M. E. *et al.* limma powers differential expression analyses for RNA-sequencing
1139   and microarray studies. *Nucleic Acids Res* **43**, e47, (2015).
1140 88   Mertens, B. J. A. Transformation, Normalization, and Batch Effect in the Analysis of Mass
1141   Spectrometry Data for Omics Studies. *Statistical Analysis of Proteomics, Metabolomics,*
1142   *and Lipidomics Data Using Mass Spectrometry*, 1-21, (2016).

1143